Publication Year	2015
Acceptance in OA@INAF	2020-04-24T13:23:36Z
Title	Radio-faint AGN: a tale of two populations
Authors	Padovani, P.; Bonzini, M.; Kellermann, K. I.; Miller, N.; Mainieri, V.; et al.
DOI	10.1093/mnras/stv1375
Handle	http://hdl.handle.net/20.500.12386/24225
Journal	MONTHLY NOTICES OF THE ROYAL ASTRONOMICAL SOCIETY
Number	452

Monthly Notices
of the
ROYAL ASTRONOMICAL SOCIETY

MNRAS **452,** 1263–1279 (2015) doi:10.1093/mnras/stv1375

Radio-faint AGN: a tale of two populations

P. Padovani,[1,2★] M. Bonzini,[1] K. I. Kellermann,[3] N. Miller,[4] V. Mainieri[1] and P. Tozzi[5]

[1]*European Southern Observatory, Karl-Schwarzschild-Str. 2, D-85748 Garching bei München, Germany*
[2]*Associated to INAF – Osservatorio Astronomico di Roma, via Frascati 33, I-00040 Monteporzio Catone, Italy*
[3]*National Radio Astronomy Observatory, 520 Edgemont Road, Charlottesville, VA 22903-2475, USA*
[4]*Department of Mathematics and Physical Sciences, Stevenson University, 1525 Greenspring Valley Road, Stevenson, MD 21153-0641, USA*
[5]*INAF – Osservatorio Astrofisico di Arcetri, Largo E. Fermi, I-50125 Firenze, Italy*

Accepted 2015 June 18. Received 2015 June 17; in original form 2015 March 6

ABSTRACT

We study the Extended *Chandra Deep Field*-South Very Large Array sample, which reaches a flux density limit at 1.4 GHz of 32.5 μJy at the field centre and redshift ∼4, and covers ∼0.3 deg^2. Number counts are presented for the whole sample while the evolutionary properties and luminosity functions are derived for active galactic nuclei (AGN). The faint radio sky contains two totally distinct AGN populations, characterized by very different evolutions, luminosity functions, and Eddington ratios: radio-quiet (RQ)/radiative-mode and radio-loud (RL)/jet-mode AGN. The radio power of RQ AGN evolves $\propto (1+z)^{2.5}$, similarly to star-forming galaxies, while the number density of RL ones has a peak at $z \sim 0.5$ and then declines at higher redshifts. The number density of radio-selected RQ AGN is consistent with that of X-ray selected AGN, which shows that we are sampling the same population. The unbiased fraction of radiative-mode RL AGN, derived from our own and previously published data, is a strong function of radio power, decreasing from ∼0.5 at $P_{1.4\,\mathrm{GHz}} \sim 10^{24}$ W Hz^{-1} to ∼0.04 at $P_{1.4\,\mathrm{GHz}} \sim 10^{22}$ W Hz^{-1}. Thanks to our enlarged sample, which now includes ∼700 radio sources, we also confirm and strengthen our previous results on the source population of the faint radio sky: star-forming galaxies start to dominate the radio sky only below ∼0.1 mJy, which is also where RQ AGN overtake RL ones.

Key words: surveys – galaxies: active – galaxies: evolution – quasars: general – galaxies: starburst – radio continuum: galaxies.

1 INTRODUCTION

Soon after the discovery of quasars (Schmidt 1963) it was realized that the majority of them were not as strong radio sources as the first quasars, as they were undetected by the radio telescopes of the time: they were 'radio-quiet' (Sandage 1965). It was later understood that these sources were actually only 'radio-faint', as for the same optical power their radio powers were ≈3–4 orders of magnitude smaller than their radio-loud (RL) counterparts, but the name stuck. Radio-quiet (RQ) active galactic nuclei (AGN) were until recently normally found in optically selected samples and are characterized by relatively low radio-to-optical flux density ratios ($R \lesssim 10$) and radio powers ($P_{1.4\,\mathrm{GHz}} \lesssim 10^{24}$ W Hz^{-1} locally).

Innumerable studies have compared the properties of the two AGN classes in various bands to try and shed light on their inherent differences. As a result, the distinction between the two types of AGN has turned out to be not simply a matter of semantics: the two classes represent intrinsically different objects, with RL AGN emitting a large fraction of their energy non-thermally and in association with powerful relativistic jets, while the multiwavelength emission of RQ AGN is dominated by thermal emission, directly or indirectly related to the accretion disc. The host galaxies are also different, with those of RL AGN being elliptical while those of RQ ones, excluding the most powerful ones, being spiral (e.g. Dunlop et al. 2003).

However, 50 years after the discovery of quasars, the question 'Why do only a minority of galaxies that contain an AGN have jets?' is still unanswered. One problem is that, while it would be important to compare the properties of the two AGN classes in the band where they differ most (i.e. the radio band), this requires the identification of AGN in deep (≲1 mJy) radio fields, as RQ AGN are, by definition, radio-faint. This has been possible only recently (e.g. Padovani et al. 2009, 2011; Simpson et al. 2012; White et al. 2015, and references therein).

Our group started addressing this topic, together with others including the broader issue of the source population in very deep radio fields, initially in the *Chandra Deep Field*-South (CDFS). This was

★ E-mail: ppadovan@eso.org

© 2015 The Authors
Published by Oxford University Press on behalf of the Royal Astronomical Society

Downloaded from https://academic.oup.com/mnras/article-abstract/452/2/1263/1062981 by guest on 16 April 2020

done by defining a complete sample of 198 radio sources reaching $\sim$43 μJy over 0.2 deg^2 at 1.4 GHz using the National Radio Astronomy Observatory (NRAO) Very Large Array (VLA) through a multiwavelength approach (Kellermann et al. 2008; Mainieri et al. 2008; Tozzi et al. 2009; Padovani et al. 2009, 2011).

Miller et al. (2008, 2013) expanded on this by observing the so-called Extended CDFS (E-CDFS), again using the VLA, down to $\sim$30 μJy at 5σ, in a 2.8 arcsec × 1.6 arcsec beam over $\sim$0.3 deg^2. This resulted in a sample of almost 900 sources. We have started exploiting these new radio data with the aim of addressing the issues of the faint radio source population and RQ AGN in more detail, given the larger and slightly deeper E-CDFS sample, as compared to the CDFS one. In particular, Bonzini et al. (2012) have identified the optical and infrared (IR) counterparts of the E-CDFS sources, finding reliable matches and redshifts for $\sim$95 and $\sim$81 per cent of them, respectively, while Vattakunnel et al. (2012) have identified the X-ray counterparts and studied the radio–X-ray correlation for star-forming galaxies (SFGs). Finally, Bonzini et al. (2013) have provided reliable source classification and studied the host galaxy properties of RQ AGN, RL AGN, and SFGs.

The main aims of this paper are as follows:

(i) to present the most accurate number counts for the various classes of sub-mJy sources down to $\sim$30 μJy;

(ii) to study the evolution and luminosity functions (LFs) of sub-mJy AGN. In particular, our CDFS paper on this topic (Padovani et al. 2011) was affected by small number statistics, particularly for RQ AGN, and by the large fraction ($\sim$50 per cent) of upper limits on the far-IR-to-radio flux density ratio (q) used for classifying sources. As discussed at length in Padovani et al. (2011), this topic has important implications for constraining the mechanism behind radio emission in RQ AGN and allow a proper comparison with RL AGN;

(iii) to investigate more deeply the density evolution of RL AGN found in Padovani et al. (2011) ($\propto (1+z)^{-1.8}$);

(iv) to provide a new approach to the issue of the fraction of RL sources within the AGN population.

Points (i) and (ii) are very relevant, together with the study of the evolution of SFGs, also to the issue of the link between the black holes at the centre of AGN and their host galaxies. Moreover, they are also critical to predict the source population at radio flux densities <1 μJy, which are important, for example, for the Square Kilometre Array. All existing estimates, in fact, had to rely, for obvious reasons, on extrapolations and are based on high flux density samples. This affects particularly the highest redshifts, which can better be probed at fainter flux densities.

Our physical definition of the various classes of sub-mJy sources follows that of Padovani et al. (2011), to which we refer the reader. Following Heckman & Best (2014) we will also use the terms 'radiative-mode' and 'jet-mode' AGN.[1] In short, radiative-mode RL AGN include radio quasars and high-excitation radio galaxies, while jet-mode RL AGN refer to low-excitation radio galaxies. There is considerable overlap between jet-mode AGN and the radio sources morphologically classified as Fanaroff–Riley type I (FR I; Fanaroff & Riley 1974) and also between RL radiative-mode AGN and FR IIs, although there is a sizeable population of jet-mode FR IIs and a smaller one of radiative-mode FR I (e.g. Gendre et al. 2013, and references therein). As for RQ AGN, radiative-mode sources are the 'classical' broad- and narrow-lined AGN (type I and II), while the jet-mode ones are the so-called liners. Note that the two classes also have widely different Eddington ratios, with radiative-mode and jet-mode sources, respectively, above and below $L/L_{\rm Edd} \approx 0.01$.

In this paper, we present the general properties (number counts, redshift distribution, etc.) of the whole sample and then concentrate on the evolution and LFs of AGN. We will discuss in detail SFGs in a future publication (Padovani et al., in preparation).

Section 2 describes the VLA-E-CDFS sample, while Section 3 presents the so-far deepest determination of sub-mJy number counts by class. Section 4 studies the sample evolution while Section 5 derives the AGN LFs and their evolution. Finally, Section 6 discusses our results, while Section 7 summarizes our conclusions. Throughout this paper, spectral indices are defined by $S_\nu \propto \nu^{-\alpha}$ and the values $H_0 = 70\,{\rm km\,s^{-1}\,Mpc^{-1}}$, $\Omega_{\rm M} = 0.3$, and $\Omega_\Lambda = 0.7$ have been used.

2 THE SAMPLE

2.1 Redshifts

Our original sample is described in Bonzini et al. (2012) and Miller et al. (2013) and includes 883 radio sources detected in 0.324 deg^2 at 1.4 GHz in a deep VLA survey of the E-CDFS. The average 5σ flux density limit is $\sim$37 μJy, reaching $\sim$30 μJy in the field centre. The fraction of sources with redshift information is $\sim$81 per cent, which is not ideal for determining the evolutionary properties and LFs of our sample. We have then excluded the outermost part of the field, where we do not have enough ancillary multiwavelength data to provide reasonable photometric redshifts. The resulting subsample covers an area of 0.285 deg^2 (see Bonzini et al. 2013, for details) and includes 765 radio sources with radio flux density ≥ 32.5 μJy, 87 per cent of which have redshifts (of these, $\sim$40 per cent are spectroscopic and $\sim$60 per cent are photometric). This is the sample we use to build the number counts in Section 3. To further increase the fraction of sources with redshift, we have made another cut and considered only sources with a 3.6 μm flux density $f_{3.6\,\mu{\rm m}} >$ 1 μJy, which is approximately the completeness limit of the IRAC observations at 3.6 μm (only four sources have $f_{3.6\,\mu{\rm m}} < 1$ μJy). Coupled with a radio flux density limit of 32.5 μJy, this provides us with clean selection criteria and with a sample of 680 radio sources, 92 per cent of which have redshift (the same fraction as in Padovani et al. 2011). We estimate the redshift for the $\sim$8 per cent of the objects in the sample without observed redshift from their $f_{3.6\,\mu{\rm m}}$, as detailed in Appendix A. To further minimize the effects of these redshift estimates, we also define two sub-samples: AGN (and RQ AGN) with $z \leq 3.66$ and SFGs with $z \leq 3.25$. Above these two values, in fact, 80 and 95 per cent of the redshifts, respectively, are estimated. By imposing such cuts, we then only assume that the excluded sources are at high redshifts, which makes sense based on their $f_{3.6\,\mu{\rm m}}$ values (see Appendix A), without actually using their values. This is the sample we use mostly to study the evolution and LF of AGN in Sections 4 and 5.

Note that the effect of these redshift estimates on our results is minimal, for two reasons: (1) our final redshift incompleteness is very small ($\sim$3, $\sim$5, and $\sim$1.5 per cent for all AGN, RQ, and RL AGN, respectively: see Section 4.1); (2) redshift affects $V_{\rm e}/V_{\rm a}$ values (Section 4.1) much less than flux density. Nevertheless, error bars on the LFs are evaluated using the number of sources per bin with redshift determination only, and when binning in redshift the percentages of estimated redshifts are also given for each bin.

[1] See table 4 of Heckman & Best (2014).

Downloaded from https://academic.oup.com/mnras/article-abstract/452/2/1263/1062981 by guest on 16 April 2020

2.2 Classification

Source classification has been done by Bonzini et al. (2013), expanding upon the scheme of Padovani et al. (2011). In short, by using $q_{24\mathrm{obs}}$, that is the logarithm of the ratio between the observed 24 μm and 1.4 GHz flux densities, we could define an 'SFG locus' based on the radio–FIR correlation for SFGs. Sources below this locus display a radio excess that is the signature of an AGN contribution to the radio luminosity and were therefore classified as RL AGN. Within and above this locus, a source was classified as a RQ AGN if there was evidence of AGN activity in the other bands considered, namely if it had a hard band (2–10 keV) X-ray luminosity greater than 10^{42} erg s^{-1} or it lay within the 'AGN wedge' of the IRAC colour–colour diagram, as defined by Donley et al. (2012). Otherwise, the object was classified as an SFG. We point out that our AGN classification includes all sources independently of optical appearance (i.e. quasar-like and galaxy-like). We refer the reader to Bonzini et al. (2013) for further details.

The issue of the classification of our sources into radiative- or jet-mode sources has been briefly discussed by Bonzini et al. (2013). The optimal approach to be able to make such a distinction requires rest-frame optical/UV emission line ratios but, given the relatively high redshift of our sample and the incomplete spectroscopic coverage, this is only possible for a handful of objects. Bonzini et al. (2013), using a criterion based on the 22 μm power proposed by Gürkan, Hardcastle & Jarvis (2014), estimated that the large majority of our RL sources are of the jet-mode type; this is confirmed by their LF (Section 5.2.1). As regards our RQ AGN, given our selection criteria, which include also a cut in X-ray power, we expect them to be for the large part of the radiative-mode type. This issue is addressed in Section 6.2.

We stress that ours is the deepest sample for which both the evolution and LFs of radio sources have been studied.

3 THE SUB-MJY NUMBER COUNTS

More than half a century ago, the earliest radio source counts gave the first indications of cosmic evolution (Ryle & Scheuer 1955), but the results were not without controversy. The central problem in understanding source counts is the conflict between source confusion at lower resolution and missing lower surface brightness sources or underestimating their flux density at high resolution. These issues, while better understood, still exist today. There is no 'correct' resolution to use that avoids the effects of confusion and resolution, but there is an optimum resolution depending on the areal density of sources. Modern deep radio surveys reach flux density levels of only a few μJy where the corresponding source density is ∼5 sources arcmin^{-2} at $S = 10\,\mu$Jy (Vernstrom et al. 2015). So a resolution of at least a few arcseconds is needed to unambiguously separate sources. But many μJy sources are typically an arcsecond in size, so are partially resolved with a 1 or 2 arcsec beam (e.g. Muxlow et al. 2005).

Published deep radio source counts are widely discrepant, even when made with the same instrument, and even with different investigators using the same instrument in the same field (Condon et al. 2012). Since source detection depends on the peak flux density, the effects of resolution cause two problems. First, if a source is resolved, the measured peak flux density needs to be multiplied by the ratio of integrated to peak flux density. For strong sources, where both the measured and peak flux densities can be accurately determined, this is straightforward. But for sources with lower signal-to-noise ratio (SNR), Gaussian fitting routines give systematically spurious large sizes and a corresponding flux density bias (e.g. Condon 1997). Even more complicated are sources where the peak flux density is below the detection limit, but with integrated flux densities which are above the detection limit. To account for these non-detections, one normally may use a source size distribution equivalent to that of stronger survey sources, but this does not necessarily give the correct answer. As described by Miller et al. (2013) we have used peak flux densities, except where we measure a significantly higher integrated value, a procedure which depends on the local SNR. Because of the then limitations of the VLA at the time of the Miller et al. (2013) survey, the 25 MHz intermediate frequency bands could be divided into only seven sub-bands each of 3.125 MHz which resulted in significant bandwidth smoothing away from the field centre. Because each source may appear in more than one subfield of the six antenna pointing mosaic, the corrections for bandwidth smoothing are not straightforward (Miller et al. 2013).

An additional problem arises when one physical source is split into two or more distinct components. Unless there is a connection between the radio features, there is no way to a priori distinguish between a relatively strong multicomponent source or multiple weaker sources. But the derived source count will depend dramatically on which interpretation is used. We have addressed this issue by reference to optical and/or X-ray counterparts using a maximum likelihood criterion to decide which optical counterparts are associated with which radio features (Bonzini et al. 2012).

Finally, we note the problem caused by the so-called Eddington bias. Because the source counts are steep, that is there are more weak sources than strong sources, random noise fluctuations cause more weak sources to appear above any flux density value than strong sources which fall below this value. As described by Wall & Jenkins (2012), the determination of the Eddington bias to the observed source count is not straightforward. Following the procedure described by Wall & Jenkins (2012), Wall (private communication) has calculated the Eddington bias corrections to the source count assuming a Euclidean slope. We then corrected the number of sources by a factor, which depended on SNR and ranged from 1/1.194 ($5 \leq \mathrm{SNR} < 6$) to 1/1.052 ($9 \leq \mathrm{SNR} < 10$). The same factors were also applied when deriving the LFs.

To investigate the relative contribution of the different source types to the radio population as a function of flux density, we consider here the sub-sample within an area of 0.285 deg^2, which provides us with more information for this purpose (i.e. we do not make any 3.6 μm flux cut). The sensitivity of our survey is a function of the position in the field of view, although a much less strong one than for the single pointing CDFS sample. In more detail, the area covered is equal to 0.285 deg^2 and independent of flux density above ∼60 μJy, decreases quite slowly to 0.279 and 0.226 deg^2 at ∼50 and ∼40 μJy, respectively, and reaches 0.05 deg^2 at the flux density limit (see Miller et al. 2013). We included sources down to a root-mean-square (rms) noise of 6.5 μJy, that is a flux density limit of 32.5 μJy.

Fig. 1(a) compares the E-CDFS number count with previous determinations at relatively high flux densities compiled by Condon (1984). The strong source count above ∼1 Jy shows the familiar steep slope resulting from the well-known dramatic evolution of RL quasars and radio galaxies. Below this value, all of the strongest sources in Universe have already been included, and the count begins to converge. Below 1 mJy, the count steepens (flattens in the normalized plot) again due to the emergence of the low-luminosity population of RQ AGN and SFGs, which are discussed further in this paper and in the next one of this series.

Downloaded from https://academic.oup.com/mnras/article-abstract/452/2/1263/1062981 by guest on 16 April 2020

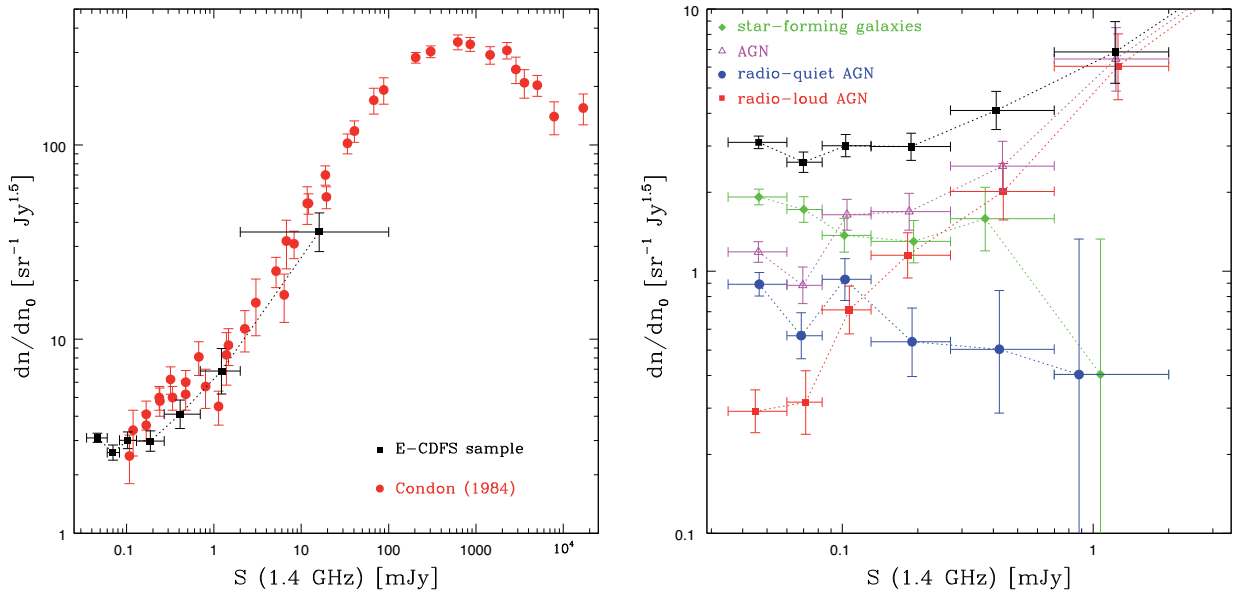

Figure 1. (a) Left: the Euclidean normalized 1.4 GHz E-CDFS source counts (black filled squares) compared to the source counts at 1.4 GHz from the compilation of Condon (1984, red filled circles). (b) Right: the Euclidean normalized 1.4 GHz E-CDFS source counts for the whole sample (black filled squares) and the various classes of radio sources: SFGs (green diamonds), all AGN (magenta triangles), RQ AGN (blue circles), and RL AGN (red squares). Error bars correspond to 1σ Poisson errors (Gehrels 1986). See the text for details.

Table 1. Euclidean normalized 1.4 GHz counts.

f_r range	Mean f_r	Counts						
		Total	SFG	Fraction	AGN	Fraction	RL AGN	RQ AGN
(μJy)	(μJy)	(sr^{-1} $Jy^{1.5}$)	(sr^{-1} $Jy^{1.5}$)	(per cent)	(sr^{-1} $Jy^{1.5}$)	(per cent)	(sr^{-1} $Jy^{1.5}$)	(sr^{-1} $Jy^{1.5}$)
32.5–60	46	$3.10^{+0.17}_{-0.16}$	$1.92^{+0.14}_{-0.13}$	62^{+6}_{-5}	$1.18^{+0.11}_{-0.10}$	38^{+4}_{-4}	$0.29^{+0.06}_{-0.05}$	$0.89^{+0.10}_{-0.09}$
60–83	70	$2.60^{+0.25}_{-0.23}$	$1.72^{+0.20}_{-0.18}$	66^{+10}_{-9}	$0.88^{+0.15}_{-0.13}$	34^{+6}_{-6}	$0.32^{+0.10}_{-0.08}$	$0.57^{+0.13}_{-0.10}$
83–130	103	$3.01^{+0.31}_{-0.28}$	$1.37^{+0.22}_{-0.19}$	46^{+8}_{-8}	$1.64^{+0.24}_{-0.21}$	54^{+9}_{-9}	$0.71^{+0.17}_{-0.14}$	$0.93^{+0.19}_{-0.16}$
130–270	188	$2.99^{+0.38}_{-0.34}$	$1.30^{+0.26}_{-0.22}$	43^{+10}_{-9}	$1.69^{+0.29}_{-0.25}$	57^{+12}_{-11}	$1.15^{+0.25}_{-0.21}$	$0.54^{+0.19}_{-0.14}$
270–700	410	$4.11^{+0.75}_{-0.64}$	$1.59^{+0.50}_{-0.39}$	39^{+14}_{-12}	$2.52^{+0.61}_{-0.50}$	61^{+18}_{-17}	$2.01^{+0.56}_{-0.45}$	$0.50^{+0.34}_{-0.22}$
700–2000	1223	$6.86^{+2.10}_{-1.65}$	$0.40^{+0.92}_{-0.33}$	6^{+13}_{-5}	$6.45^{+2.05}_{-1.59}$	94^{+37}_{-37}	$6.05^{+2.00}_{-1.54}$	$0.40^{+0.92}_{-0.33}$
2000–100 000	16 092	$35.6^{+9.1}_{-7.4}$	–	–	$35.6^{+9.1}_{-7.4}$	100^{+33}_{-33}	$35.6^{+9.1}_{-7.4}$	–

Table 1 and Fig. 1(b)[2] present the Euclidean normalized number counts for the various classes. The normalized number counts agree very well in the region of overlap (flux densities ≥43 μJy) with those of the CDFS (Kellermann et al. 2008)[3] and appear to be slightly higher at fainter flux densities. The comparison with the number counts of Padovani et al. (2011) is not shown for clarity but the two determinations agree very well, typically within $\sim 1\sigma$. The main results of Padovani et al. (2011) are also confirmed: AGN dominate at large flux densities ($\gtrsim$1 mJy) but SFGs become the dominant population below ≈0.1 mJy. Similarly, RL AGN are the predominant type above 0.1 mJy but their counts drop fast at lower values.

In more detail, AGN make up 43 ± 3 per cent (where the errors are based on binomial statistics: Gehrels 1986) of sub-mJy sources and their counts are seen to drop at lower flux densities, going from 100 per cent of the total at ∼10 mJy down to 38 per cent at the survey limit. SFGs, on the other hand, which represent 57 ± 4 per cent of the sample, are missing at high flux densities but become the dominant population below ≈0.1 mJy, reaching 62 per cent at the survey limit. RQ AGN represent 26 ± 2 per cent (or 61 per cent of all AGN) of sub-mJy sources but their fraction appears to increase at lower flux densities, where they make up 75 per cent of all AGN and ≈29 per cent of all sources at the survey limit, up from ≈6 per cent, respectively, at ≈1 mJy. The relative fractions of the various classes in our sample are shown in fig. 6 of Bonzini et al. (2013).

[2] A preliminary version of this figure has been shown by Padovani et al. (2014).

[3] Due to a small numerical error, the number counts in Kellermann et al. (2008) and, consequently, also those in Padovani et al. (2009, 2011) were too high by ∼5 per cent.

4 EVOLUTION

4.1 V_e/V_a analysis

We first study the evolutionary properties of the VLA-E-CDFS sample through a variation of the V/V_{max} test (Schmidt 1968), the V_e/V_a test (Avni & Bahcall 1980; Morris et al. 1991), that is the ratio between *enclosed* and *available* volume, since we do not have a single flux density limit (see Section 3). More details on this and other statistical techniques used in this paper can be found in Padovani et al. (2011).

Downloaded from https://academic.oup.com/mnras/article-abstract/452/2/1263/1062981 by guest on 16 April 2020

Table 2. Sample evolutionary properties: V_e/V_a analysis.

Sample	N	$\langle z \rangle$	Est. z (per cent)	$\langle V_e/V_a \rangle$	p-value	k_L[a]	k_D[b]
All sources	680	1.35 ± 0.05	8.4	0.609 ± 0.011	<0.001	1.6 ± 0.1	–
Star-forming galaxies	372	1.16 ± 0.05	8.9	0.656 ± 0.015	<0.001	2.1 ± 0.1	–
Star-forming galaxies, $z \leq 3.25$	356	1.01 ± 0.04	5.1	0.651 ± 0.015	<0.001	2.4 ± 0.2	–
All AGN	308	1.54 ± 0.08	7.8	0.550 ± 0.016	<0.001	0.9 ± 0.2	–
All AGN, $z \leq 3.66$	288	1.27 ± 0.05	2.8	0.552 ± 0.017	0.003	1.1 ± 0.3	–
All AGN, $z \leq 3.66$, no LSS	264	1.31 ± 0.05	3.0	0.556 ± 0.018	0.003	1.2 ± 0.3	–
RQ AGN	172	1.93 ± 0.11	12.8	0.709 ± 0.022	<0.001	2.3 ± 0.1	–
RQ AGN, $z \leq 3.66$	155	1.54 ± 0.07	5.2	0.708 ± 0.023	<0.001	3.0 ± 0.2	–
RQ AGN, $z \leq 3.66$, no LSS	141	1.61 ± 0.08	5.7	0.711 ± 0.024	<0.001	3.0 ± 0.2	–
RL AGN	136	1.00 ± 0.06	1.5	0.354 ± 0.025	<0.001	-3.9 ± 0.9	-2.1 ± 0.3
RL AGN, no LSS	126	1.03 ± 0.07	1.6	0.362 ± 0.026	<0.001	-3.6 ± 0.9	-2.0 ± 0.3

Notes. [a]Pure luminosity evolution $P(z) = P(0)(1+z)^{k_L}$.
[b]Pure density evolution $\Phi(z) = \Phi(0)(1+z)^{k_D}$.

We have computed V_e/V_a values for our sources taking into account our double flux density limits and the appropriate sky coverage (see equations 42 and 43 of Avni & Bahcall 1980). The IR k-correction was done by using the measured near-IR spectral indices. In the radio band, spectral indices between 1.4 and 4.86 GHz are available for ∼29 per cent of the sources (Kellermann et al. 2008; Huynh et al. 2012), while for the rest the mean values for the relevant classes were assumed. Statistical errors are given by $\sigma = 1/\sqrt{12\,N}$ (Avni & Bahcall 1980). We estimate the significance of the deviation from the non-evolutionary case by deriving the p-value that the V_e/V_a distribution is similar to a uniform one according to a Kolmogorov-Smirnov (KS) test. Similar results are obtained by using the deviation from 0.5 (the value expected for no evolution) of $\langle V_e/V_a \rangle$. To have an initial simple estimate of the sample evolution, we have also derived the best-fitting parameter k_L assuming a pure luminosity evolution (PLE) of the type $P(z) = P(0)(1+z)^{k_L}$ or a pure density evolution (PDE) of the type $\Phi(z) = \Phi(0)(1+z)^{k_D}$, where $\Phi(z)$ is the LF.

Our results are shown in Table 2, which gives the sample in column (1), the number of sources in column (2), the mean redshift in column (3), the percentage of sources with redshift estimated from the magnitude in column (4), $\langle V_e/V_a \rangle$ in column (5), the p-value that the V_e/V_a distribution is similar to a uniform one in column (6), and the best-fitting parameters k_L and k_D (when applicable) in columns (7) and (8), respectively. When the best fit indicates negative luminosity evolution (i.e. $k_L < 0$), in fact, we fit a PDE model as well, which we feel is more physical in this case. The mean redshift is calculated taking into account the effect of the sky coverage, that is each object is weighted by the inverse of the area accessible at the flux density of the source (e.g. Padovani et al. 2007).

The fractional redshift distributions for the different classes are shown in Fig. 2. As also shown in Table 2, RQ AGN have the highest $\langle z \rangle$ ($z \sim 2$) and reach $z \sim 6$–7 (photometric redshifts). RL AGN have also a relatively broad distribution, extending up to $z \sim 4.5$ but with a lower $\langle z \rangle$ than RQ ones ($z \sim 1$). SFGs are in between but closer to RL AGN. The main results on the sample evolution are the following.

(i) The whole sample has $\langle V_e/V_a \rangle > 0.5$ and shows significant evolution characterized by $k_L = 1.6 \pm 0.1$.

(ii) SFGs evolve at a very high significance level (p-value <0.001); their evolutionary parameter for the case of PLE is $k_L = 2.1 \pm 0.1$. This increases to $k_L = 2.4 \pm 0.2$ for a redshift cut $z \leq 3.25$, which reduces the fraction of estimated redshifts.

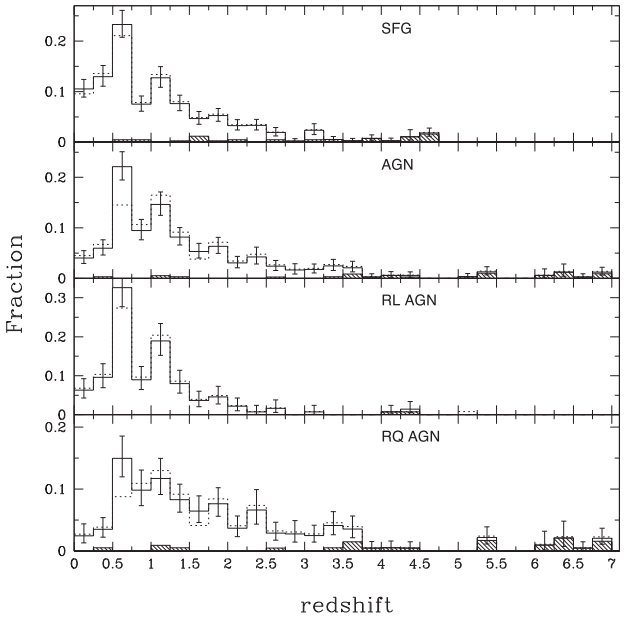

Figure 2. Fractional redshift distributions for the different classes of sources, deconvolved with the appropriate sky coverage. The dashed areas denote redshifts estimated from the 3.6 μm flux density. Error bars represent the 1σ range based on Poisson statistics. The dotted lines take into account the presence of LSS as discussed in Appendix B.

The evolution and LF of SFGs will be presented and discussed in Padovani et al. (in preparation).

(iii) AGN as a whole evolve relatively weakly, with $k_L = 0.9 \pm 0.2$ ($k_L = 1.1 \pm 0.3$ for $z \leq 3.66$).

(iv) RQ AGN, however, evolve very significantly (p-value < 0.001) with $k_L = 2.3 \pm 0.1$, consistent with the value of SFGs [a thorough comparison between the two classes is deferred to Padovani et al. (in preparation)]. This increases to $k_L = 3.0 \pm 0.2$ for a redshift cut $z \leq 3.66$, which reduces the fraction of estimated redshifts.

(v) RL AGN also evolve strongly (p-value < 0.001) but in the negative sense, with $k_L = -3.9 \pm 0.9$ and $k_D = -2.1 \pm 0.3$. This evolution is in the opposite sense as that of RQ AGN. As we show below (Sections 4.2 and 5.2.2), the best-fitting evolution of RL AGN is more complicated than assumed here.

Downloaded from https://academic.oup.com/mnras/article-abstract/452/2/1263/1062981 by guest on 16 April 2020

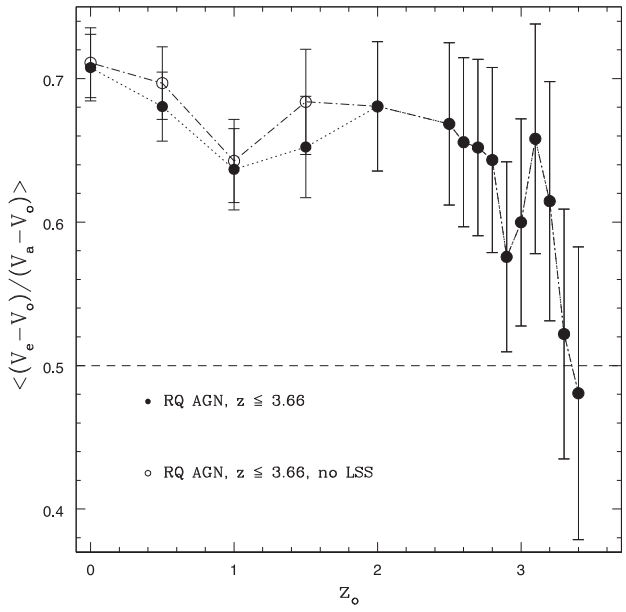

Figure 3. The banded statistic $\langle (V_e - V_o)/(V_a - V_o)\rangle$ versus z_o, for our RQ AGN with $z \leq 3.66$. The horizontal dashed line indicates the value of 0.5, expected under the null hypothesis of no evolution. Open symbols take into account the presence of LSS as discussed in Appendix B.

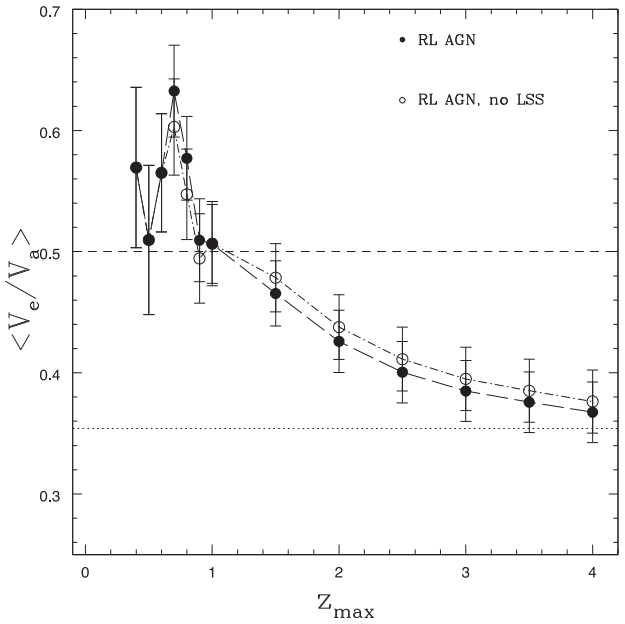

Figure 4. $\langle V_e/V_a\rangle$ as a function of maximum redshift for our RL AGN. The horizontal dashed line indicates the value of 0.5, expected under the null hypothesis of no evolution, while the dotted line is the value for the sample. Open symbols take into account the presence of LSS as discussed in Appendix B.

We note that Padovani et al. (2011) found a difference in $\langle V_e/V_a\rangle$ between RL AGN with powers below and above $P = 10^{24.5}$ W Hz^{-1}, with the former having $\langle V_e/V_a\rangle \approx 0.5$ and the latter reaching smaller values. Given the flux density-limited nature of our sample, and the resulting degeneracy between power and redshift, we believe that this difference, which is still present in the current sample, is better characterized as a redshift dependence (see Section 5.2.2).

Given the small area of our survey, one could worry that the presence of large-scale structures (LSS; e.g. Gilli et al. 2003) and related redshift spikes might influence some of our results. The LSS in the E-CDFS is discussed in Appendix B. To assess the impact of the LSS on our study, most of our results are presented for the 'full' and the 'no LSS' sub-samples, as illustrated, for example, in Fig. 2 (cf. the solid with the dotted lines). As shown in Table 2, the resulting $\langle V_e/V_a\rangle$ values and best-fitting evolutionary parameters for the latter are well within 1σ from those derived for the former, which shows that the effect of the LSS on these results is minimal. These overdensities are obviously more noticeable when one studies the evolution of the LF with redshift (see, e.g., the top-middle and bottom-left panels of Fig. 9) but even then the revised LFs are typically within $\lesssim 1\sigma$ from the 'full' ones.

4.2 The banded $\langle V_e/V_a\rangle$

Given the available statistics, we can easily study possible changes of the evolution with redshift by using the so-called banded $\langle V/V_{max}\rangle$ statistic, i.e. the quantity $\langle (V - V_o)/(V_{max} - V_o)\rangle$ or $\langle (V_e - V_o)/(V_a - V_o)\rangle$ in our case, where V_o is the cosmological volume enclosed by a given redshift z_o (Dunlop & Peacock 1990). This procedure allows us to detect any high-redshift (possibly negative) evolution by separating it by the well-known strong (positive) low-redshift evolution.

Fig. 3 shows that $\langle (V_e - V_o)/(V_a - V_o)\rangle$ for RQ AGN has a very slow decline with redshift, but still with values significantly >0.5, until it reaches 0.5 at $z \approx 3.3$. This suggests that the evolution might be somewhat weaker at higher redshifts; we will address this in Sections 5.3.2 and 6.1.2.

As for the RL AGN $\langle V_e/V_a\rangle$ is <0.5 for the whole sample, so the banded $\langle V/V_{max}\rangle$ statistic is not useful. However, we can plot $\langle V_e/V_a\rangle$ versus the maximum redshift of the sub-sample to see if there is evidence of positive or at least null evolution at low redshifts. This is done in Fig. 4, which shows that, indeed, up to $z \approx 1.5$ $\langle V_e/V_a\rangle$ is not significantly <0.5, being actually >0.5 at the $\sim 2\sigma$–3σ level at $z \sim 0.7$–0.8. While part of this is due to the presence of LSS, taking these into account still results in $\langle V_e/V_a\rangle \sim 0.5$ and actually >0.5 at the 2.6σ level at $z \sim 0.7$. At $z > 1$, $\langle V_e/V_a\rangle$ declines with redshift, reaching gradually its sample value. This shows that the RL AGN evolution changes from being positive/null to being negative around $z \approx 1$–1.5 and that therefore it cannot be characterized by a simple $(1 + z)^k$ law. In other words, $\langle V_e/V_a\rangle$ evaluated for the whole sample tells only part of the story. We will expand on this in Section 5.2.2.

4.3 Maximum likelihood analysis

A more general approach to estimate the evolution, and at the same time the LF, is to perform a maximum likelihood fit of an evolving LF to the observed distribution in luminosity and redshift. This approach makes maximal use of the data and is free from arbitrary binning; however, unlike the V_e/V_a test, it is model dependent. We consider single and double power-law LFs, that is $\Phi(P) \propto P^{-\gamma_1}$ and $\Phi(P) \propto 1/[(P/P_*)^{\gamma_1} + (P/P_*)^{\gamma_2}]$, respectively, with a break at P_*. We refer the reader to Padovani et al. (2011) for more details.

Our results are shown in Table 3, which gives the sample in column (1), the evolutionary model in column (2), the two LF slopes (if applicable) in columns (3) and (4), the best-fitting evolutionary parameter in column (5), and the break power (if applicable) in column (6). Errors are 1σ for one interesting parameter. The

Downloaded from https://academic.oup.com/mnras/article-abstract/452/2/1263/1062981 by guest on 16 April 2020

Table 3. Sample LFs and evolution: maximum likelihood analysis best fits. We consider an LF of the type $\Phi(P) \propto 1/[(P/P_*)^{\gamma_1} + (P/P_*)^{\gamma_2}]$ and an evolution $\propto (1+z)^k$. KS_z and KS_P are the KS p-values for the redshift and radio power distributions, respectively.

Sample	Model	γ_1	γ_2	k	$\log P_*$ (W Hz^{-1})	KS_z	KS_P
AGN, $z \leq 3.66$	PDE	1.70 ± 0.04	–	0.11 ± 0.26	–	<0.001	0.016
AGN, $z \leq 3.66$	PLE	1.70 ± 0.04	–	$0.16^{+0.33}_{-0.41}$	–	<0.001	0.016
AGN, $z \leq 3.66$	PDE	$1.2^{+0.1}_{-0.2}$	1.82 ± 0.06	0.0 ± 0.3	22.6 ± 0.6	0.006	0.306
AGN, $z \leq 3.66$	PLE	1.2 ± 0.2	1.80 ± 0.05	-0.15 ± 0.35	22.6 ± 0.6	0.005	0.340
AGN, $z \leq 3.66$, no LSS	PLE	1.3 ± 0.2	$1.80^{+0.10}_{-0.05}$	0.1 ± 0.4	$22.5^{+1.2}_{-0.9}$	0.039	0.383
RQ AGN, $z \leq 3.66$	PLE	2.3 ± 0.1	–	2.8 ± 0.2	–	0.022	0.038
RQ AGN, $z \leq 3.66$	**PLE**	$0.6^{+0.6}_{-0.7}$	$2.64^{+0.19}_{-0.27}$	$2.52^{+0.20}_{-0.23}$	$22.32^{+0.20}_{-0.16}$	0.372	0.885
RQ AGN, $z \leq 3.66$, no LSS	**PLE**	$0.9^{+0.5}_{-0.6}$	$2.72^{+0.25}_{-0.23}$	2.54 ± 0.23	22.50 ± 0.25	0.471	0.879
RL AGN	PLE	$1.40^{+0.05}_{-0.04}$	–	-6.0 ± 1.4	–	0.003	0.771
RL AGN	PDE	1.40 ± 0.04	–	-2.4 ± 0.3	–	0.003	0.772
RL AGN, no LSS	PDE	1.41 ± 0.04	–	-2.3 ± 0.3	–	0.018	0.870

Note. Models consistent with the data are indicated in boldface.

best-fitting evolutionary parameters agree (within 1σ–2σ) with those derived through the V_e/V_a approach.

The maximum likelihood approach (but also the V_e/V_a one) does not provide a goodness-of-fit test. Therefore, as is typically done, we carry out a KS test on both the cumulative redshift and radio power distributions and compute the probability of having the KS test statistics as large or larger than the observed one. This can be used to reject a model when too low. The p-values are given in columns (7) (KS_z) and (8) (KS_P), respectively, where the $>2\sigma$ and $>3\sigma$ levels correspond to values <0.046 and <0.003, respectively. The fact that in most cases one of the two p-values is $\leq$0.04 shows that the models we adopted are too simplistic, as detailed in the next section.

5 LUMINOSITY FUNCTIONS

The results of the maximum likelihood approach expand upon and complement those of the V_e/V_a test. A single power-law fit for the LF of AGN is excluded with very high significance (p-value <0.001), both in the case of PLE and PDE. However, even a double power-law fit is inconsistent with the data, which means that the adopted evolutionary laws are too simple. A single power-law fit for the LF of RQ AGN is also excluded (p-value ∼0.02), while a PLE evolution plus a double power-law LF is consistent with the data. As for RL AGN, neither a simple PLE or PDE model can fit the data, while a double power-law LF is not needed (the best-fitting slopes turn out to be the same well within the errors). The two AGN classes, apart from displaying evolutions with different signs, also have widely different LF shapes, with RL AGN being characterized by a much flatter LF. Note that the effect of the LSS on these results is truly minimal ($<1\sigma$).

We now turn to study the AGN LFs in more detail. We first study all AGN together but then, given their widely different LFs and evolutions, we examine the two classes separately.

The effect of cosmic variance was included in the LF uncertainties as follows. (1) We first estimated σ_{dm} for the relevant redshift range following Moster et al. (2011, using the IDL code provided in their paper). (2) We then derived the bias b for the appropriate redshift and number density from fig. 3 (left) of Somerville et al. (2004). We could not use in fact Moster et al. (2011) to get b as well given that their numbers apply to the whole galaxy population above a given stellar mass, while we here deal with a radio-selected sample. (3) We estimated the relative cosmic variance as $\sigma_v = b \times \sigma_{dm}$ (see Moster et al. 2011, for details and definitions). (4) σ_v was then added in quadrature with the Poisson uncertainties for each subpopulation in each redshift bin. We note that, since the number of objects per power bin in our LFs is never very large, the former turned out always to be smaller than the latter.

5.1 All AGN

Fig. 5 shows three different estimates of the local LF for our AGN, done using the $1/V_{max}$, or in our case $1/V_a$, method. The AGN $z \leq 0.4$ sample, which includes 29 objects, is consistent with no evolution ($\langle V_e/V_a \rangle = 0.57 \pm 0.05$) and can therefore be used as a robust proxy for the local AGN LF (filled squares; similar results are obtained by using the $z \leq 0.3$ sample, which however contains only 21 objects). To increase our statistics, we have included in the sample all sources above our radio completeness limit independently of their $f_{3.6\,\mu m}$ values (see Section 2.1), which adds four more sources.[4] In Fig. 5, we also plot the best fits to the local ($z \leq 0.3$) LFs from Sadler et al. (2002) and Mauch & Sadler (2007) (dotted and dash–dotted lines, respectively). Our local LF is consistent within the errors ($\chi^2_\nu \lesssim 1.5$) with both but nominally a factor of ∼1.7–2.3 higher than the Sadler et al. (2002) and Mauch & Sadler (2007) LF, respectively.

Our $z < 0.4$ LF agrees with the $z < 0.2$ AGN LF of Mao et al. (2012), based on the Australia Telescope Large Area Survey (ATLAS) at 1.4 GHz, which currently reaches ∼150 μJy per beam. The Smolčić et al. (2009) AGN LF in the 0.1–0.35 redshift range (not shown for clarity) is also consistent with ours.

Fig. 5 shows two further estimates of the local LF for E-CDFS AGN, which are based on the whole sample but are model dependent. The first one is the LF de-evolved to $z = 0$ (filled circles) using the best-fitting evolutionary parameter from the $\langle V_e/V_a \rangle$ analysis. This LF is not consistent ($\chi^2_\nu \sim 6.1$–8.2, respectively, p-value <0.0001) with both previous LFs, which indicates that the redshift evolution is more complex than assumed. The situation does not change taking into account the LSS ($\chi^2_\nu \sim 5.0$–6.2, p-value <0.0001). The second one is the LF derived from the maximum likelihood analysis (double power-law fit, PLE), including

[4] We do not need in fact to restrict ourselves to sources with $f_{3.6\,\mu m} > 1$ μJy to increase redshift completeness, since none of the AGN with $z < 0.4$ have redshift estimated from $f_{3.6\,\mu m}$.

Downloaded from https://academic.oup.com/mnras/article-abstract/452/2/1263/1062981 by guest on 16 April 2020

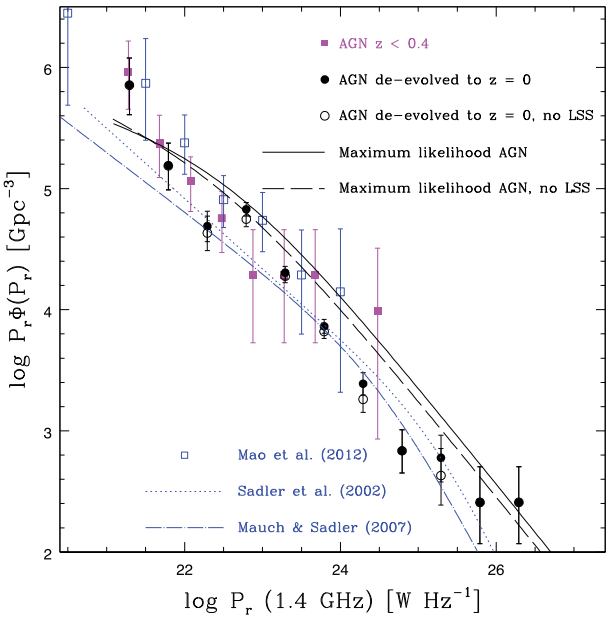

Figure 5. The local differential 1.4 GHz LF for AGN in a $P \times \phi(P)$ form. Filled (magenta) squares indicate the E-CDFS LF at $z \leq 0.4$, while filled (black) circles denote the LF de-evolved to $z = 0$ using the best-fitting evolutionary parameter from the $\langle V_e/V_a \rangle$ analysis, with open circles taking into account the presence of LSS. The solid line is the best-fitting double power-law LF from the maximum likelihood method (PLE), while the dashed line is the same LF but taking into account the presence of LSS. Open (blue) squares refer to the $z < 0.2$ ATLAS LF (Mao et al. 2012). The best fits to the local AGN LF from Sadler et al. (2002, converted to our value of H_0) and Mauch & Sadler (2007) are also shown (blue dotted and dash–dotted lines, respectively). Error bars for the E-CDFS $z \leq 0.4$ sample correspond to 1σ Poisson errors evaluated using the number of sources per bin with redshift determination added in quadrature with the cosmic variance uncertainties.

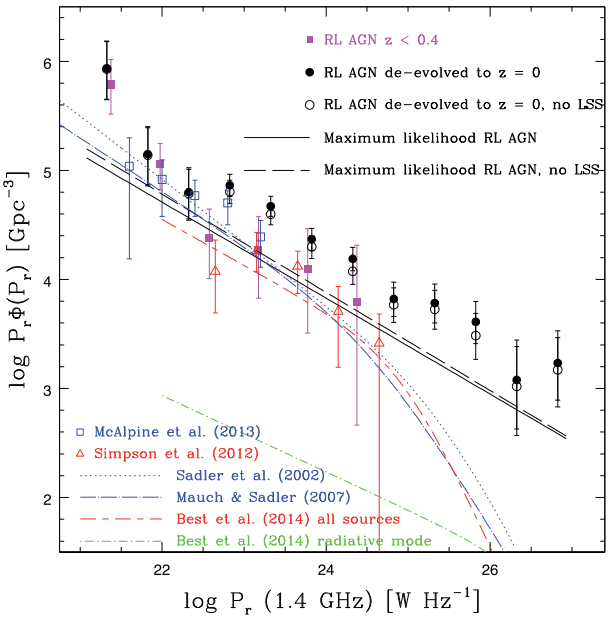

Figure 6. The local differential 1.4 GHz LF for RL AGN in a $P \times \phi(P)$ form. Filled (magenta) squares indicate the E-CDFS LF at $z \leq 0.4$, while filled (black) circles denote the LF de-evolved to $z = 0$ using the best-fitting evolutionary parameter from the $\langle V_e/V_a \rangle$ analysis, with open circles taking into account the presence of LSS. The solid line is the best fit from the maximum likelihood method (ZDE), while the dashed line is the same LF but taking into account the presence of LSS. Open (blue) squares refer to the $0.05 < z < 0.35$ VIDEO-*XXM3* LF (McAlpine, Jarvis & Bonfield 2013), while open (red) triangles are the $z \leq 0.5$ Subaru/*XMM–Newton Deep Field* LF (Simpson et al. 2012), corrected to take into account the different selection criteria as described in the text. The best fits to the local AGN LF from Sadler et al. (2002) (converted to our value of H_0), Mauch & Sadler (2007) (blue dotted and dash–dotted lines, respectively), and Best et al. (2014) (all sources: red short–long dashed line; radiative-mode: green dot–short-dashed line) are also shown. Error bars for the E-CDFS $z \leq 0.4$ sample correspond to 1σ Poisson errors evaluated using the number of sources per bin with redshift determination added in quadrature with the cosmic variance uncertainties.

also the LSS effect, which is ∼2–3 times higher than previous determinations.

This situation is somewhat at variance with that in Padovani et al. (2011), where the local AGN LF was different (p-value ∼0.011) from both the Sadler et al. (2002) and Mauch & Sadler (2007) LF. We attribute this difference to a statistical fluctuation due to the smaller (15 sources versus 29) local AGN sample available in that paper. As regards the fact that our LFs are still somewhat higher than previous LFs, we noted in Padovani et al. (2011) that our AGN LF includes the contribution of RQ AGN, which were not present in significant numbers in these two LFs as these were based on the NRAO VLA Sky Survey ($S_{\rm min} \gtrsim 2.8$ mJy), while RQ AGN make up a non-negligible fraction of radio sources only below ≈1 mJy (Fig. 1). Moreover, both previous LFs included only non-stellar optical sources (i.e. they excluded quasars), while we have no such cut. The issue of the RQ AGN contribution can be dealt with by studying RL AGN only.

5.2 RL AGN

5.2.1 The local LF

Fig. 6 shows three different estimates of the local LF for our RL AGN. The RL AGN $z \leq 0.4$ sample, which includes 23 objects, is consistent with no evolution ($\langle V_e/V_a \rangle = 0.57 \pm 0.06$) and can therefore be used as a robust proxy for the local RL AGN LF (filled squares). As done for the full AGN sample, this includes all sources above our radio completeness limit independently of their $f_{3.6\,\mu\rm m}$ values (see Section 2.1). Our local LF is consistent within the errors ($\chi^2_\nu \lesssim 1.3$) with both the LFs from Sadler et al. (2002) and Mauch & Sadler (2007) (dotted and dash–dotted lines, respectively), although still a factor of ∼1.4–1.8 higher.

We also compare our local LF with the $z \leq 0.5$ Subaru/*XMM–Newton Deep Field* LF of Simpson et al. (2012, red open triangles). That paper adopts a somewhat different method to classify AGN into RL and RQ sources, based on the rest-frame ratio of mid-IR to radio flux density $q_{24} = \log(S_{24\,\mu\rm m}/S_{1.4\,\rm GHz})$, with RL AGN defined by $q_{24} \leq -0.23$. Our method relies instead on the observed q_{24} and the dividing line is redshift dependent. To take this difference into account, we checked how many RL AGN with $z \leq 0.5$ and flux density ≥100 μJy (the limit of Simpson et al. 2012) were classified as RL AGN by our method and by that of Simpson et al. (2012) and corrected their LF by the ratio of the two numbers (1.6). After doing this, the two LFs are in perfect agreement. Note that Del Moro et al. (2013) have also shown that $q_{24} \leq -0.23$ gives an incomplete selection of RL AGN as it misses evidence for radio jets.

We also include the $0.05 < z < 0.35$ VIDEO-*XXM3* LF of McAlpine et al. (2013, blue open squares), who selected their

Downloaded from https://academic.oup.com/mnras/article-abstract/452/2/1263/1062981 by guest on 16 April 2020

Table 4. RL AGN LF and Evolution: ZDE maximum likelihood analysis best fits. We consider an LF of the type $\Phi(P) \propto P^{-\gamma_1}$ and an evolution peaking at $z_{\rm peak}$, which is $\propto (1+z)^{k_{\rm low}}$ and $\propto (1+z)^{k_{\rm high}}$ at low and high redshifts, respectively (see equation 1). KS_z and KS_P are the KS p-values for the redshift and radio power distributions, respectively.

Sample	γ_1	$k_{\rm low}$	$k_{\rm high}$	$z_{\rm peak}$	KS_z	KS_P
RL AGN	1.44 ± 0.04	$2.2^{+1.8}_{-1.6}$	$-3.9^{+0.7}_{-0.8}$	0.49 ± 0.10	0.331	0.889
RL AGN, no LSS	1.45 ± 0.05	$1.4^{+2.0}_{-1.2}$	$-3.7^{+0.8}_{-1.4}$	0.41 ± 0.18	0.524	0.872

AGN based on them being in host galaxies 'redder than the spiral galaxy templates' (and therefore are most likely going to be of the RL type). Their LF appears to be somewhat higher than ours at $P \approx 10^{23}$ W Hz^{-1} but the difference in selection criteria between the two derivations makes a more detailed comparison difficult.

Finally, Fig. 6 shows also two more LFs: the $z < 0.3$ LF of Best et al. (2014) for all sources (red short–long dashed line) and radiative-mode only (green dot–short-dashed line). Our local LF is consistent with the first LF although nominally a factor of ∼1.3 higher. We discuss this, together with the general issue of comparing our LFs to many previous derivations, in Section 6.1.1. Our LF is ∼2 orders of magnitude higher than the radiative-mode radio AGN LF, which confirms the fact that the bulk of our RL AGN are of the jet-mode type (see also Section 6.2).

Fig. 6 also shows two further estimates of the local LF for E-CDFS RL AGN, which are based on the whole sample but are model dependent. The first one is the LF de-evolved to $z = 0$ (filled circles) using the best-fitting evolutionary parameter for PDE from the $\langle V_e/V_a \rangle$ analysis. This LF is totally inconsistent (p-value <0.0001) with both previous LFs, which indicates that the redshift evolution is more complex than assumed. (The situation does not change taking into account the LSS: p-value <0.0001.) This is confirmed by the second one, that is the LF derived from the maximum likelihood analysis using a more complex density evolutionary law than PDE, as detailed in Section 5.2.2. In this case, the best-fitting LF is in good agreement with both previous LFs up to $P \gtrsim 10^{24}$ W Hz^{-1}, which suggests that this evolutionary law might be valid only up to these powers, as we cannot yet constrain the bright-end slope of the LF (this has however been done by other wider/shallower surveys).

5.2.2 *The LF redshift evolution*

We noticed in Section 4.2 that the RL AGN evolution cannot be simply parametrized by a $(1+z)^k$ law but reaches a peak at $z \approx 0.5$–1. We therefore introduce a more complex density evolutionary law, which we term as '$z_{\rm peak}$ density evolution' (ZDE) as follows:

$$\mathrm{ev}(z) = \frac{(1+z_{\rm c})^{k_{\rm low}} + (1+z_{\rm c})]^{k_{\rm high}}}{[(1+z_{\rm c})/(1+z)]^{k_{\rm low}} + [(1+z_{\rm c})/(1+z)]^{k_{\rm high}}}. \quad (1)$$

This allows for a situation where evolution changes sign above some redshift and for a smooth transition. Indeed, $\mathrm{ev}(z) \propto (1+z)^{k_{\rm low}}$ and $\mathrm{ev}(z) \propto (1+z)^{k_{\rm high}}$ for $z \ll z_{\rm c}$ and $z \gg z_{\rm c}$, respectively (and $\mathrm{ev}(0) = 1$). If $k_{\rm low} > 0$ and $k_{\rm high} < 0$, then $\mathrm{ev}(z)$ peaks at $z_{\rm peak} = (-k_{\rm high}/k_{\rm low})^{1/(k_{\rm high}-k_{\rm low})}(1+z_{\rm c}) - 1$. The results of fitting this model to our RL AGN sample are reported in Table 4. We find a best-fitting $z_{\rm peak} \sim 0.5$, with the density evolution turning from positive to negative, respectively, below and above this value, while the slope of the LF is basically the same as derived before. Importantly, the model is consistent with the data as shown by the results of both KS tests. Taking into account the effects of the LSS changes our best-fitting parameters by less than 1σ.

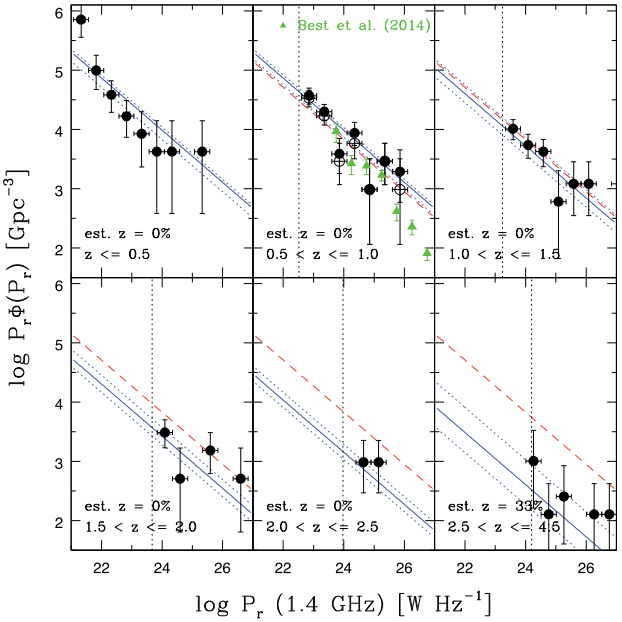

Figure 7. The differential 1.4 GHz LF for RL AGN in a $P \times \phi(P)$ form in six redshift bins. The (blue) solid lines represent the best-fitting single power-law LF from the maximum likelihood method (ZDE) evolved to the central redshift of the bin using the best fit for the complex density evolution described in Section 5.2.2, with dotted lines showing the same LF at the two extreme redshifts defining the bin. The (red) short-dashed line represents the best-fitting LF at $z = 0$. Error bars correspond to 1σ Poisson errors evaluated using the number of sources per bin with redshift determination added in quadrature with the cosmic variance uncertainties. The percentage of redshifts estimated from $f_{3.6\,\mu\rm m}$ is also given for each bin. Open symbols in the $z = 0.5$–1.0 bin take into account the presence of LSS, while (green) triangles are the LF from Best et al. (2014, all sources). The dotted vertical lines denote the completeness limit in power for each redshift range. See the text for details.

Fig. 7 (tabulated in Table 5) shows the evolution of the RL AGN LF in six redshift bins. The decrease in number at higher redshifts is clearly visible, as is the fact that the ZDE maximum likelihood fit provides a very good representation of the LF redshift evolution.

As discussed in Section 6.1.1, a direct comparison between the evolution of our LF and previously published results is not straightforward. However, once one takes into account some of the most obvious differences, our results are in agreement with previous ones. As an example, Fig. 7 shows that our LF in the 0.5–1.0 redshift bin is somewhat higher than, as expected, but still consistent within the errors with, that of Best et al. (2014, all sources). The same thing applies to the LFs of Gendre, Best & Wall (2010) in the 0.8–1.5 and 1.2–2.5 bins.

Downloaded from https://academic.oup.com/mnras/article-abstract/452/2/1263/1062981 by guest on 16 April 2020

Table 5. LFs of VLA-E-CDFS RL AGN.

z range	$\log P_{1.4\,\mathrm{GHz}}$ (W Hz^{-1})	$\log P\Phi(P)$ (Gpc^{-3})	N
	21.33	$5.85^{+0.26}_{-0.30}$	4
	21.83	$4.99^{+0.26}_{-0.32}$	4
	22.33	$4.58^{+0.23}_{-0.30}$	5
$z \leq 0.5$	22.83	$4.22^{+0.26}_{-0.35}$	4
	23.33	$3.93^{+0.37}_{-0.56}$	2
	23.83	$3.62^{+0.52}_{-1.04}$	1
	24.33	$3.62^{+0.52}_{-1.04}$	1
	25.33	$3.62^{+0.52}_{-1.04}$	1
	22.85	$4.57^{+0.13}_{-0.14}$ ($4.53^{+0.13}_{-0.15}$)	18 (16)
	23.35	$4.30^{+0.12}_{-0.14}$ ($4.23^{+0.13}_{-0.16}$)	20 (17)
	23.85	$3.59^{+0.26}_{-0.33}$ ($3.46^{+0.30}_{-0.39}$)	4 (3)
$0.5 < z \leq 1.0$	24.35	$3.94^{+0.18}_{-0.21}$ ($3.76^{+0.21}_{-0.26}$)	9 (6)
	24.85	$2.99^{+0.52}_{-0.93}$	1
	25.35	$3.46^{+0.30}_{-0.39}$	3
	25.85	$3.29^{+0.37}_{-0.52}$ ($2.99^{+0.52}_{-0.93}$)	2 (1)
	23.59	$4.01^{+0.15}_{-0.18}$	13
	24.09	$3.74^{+0.18}_{-0.22}$	9
$1.0 < z \leq 1.5$	24.59	$3.63^{+0.20}_{-0.25}$	7
	25.09	$2.78^{+0.52}_{-0.96}$	1
	25.59	$3.08^{+0.37}_{-0.54}$	2
	26.09	$3.08^{+0.37}_{-0.54}$	2
	24.09	$3.49^{+0.21}_{-0.26}$	6
$1.5 < z \leq 2.0$	24.59	$2.71^{+0.52}_{-0.90}$	1
	25.59	$3.18^{+0.30}_{-0.39}$	3
	26.59	$2.71^{+0.52}_{-0.90}$	1
	24.65	$2.98^{+0.37}_{-0.52}$	2
$2.0 < z \leq 2.5$	25.15	$2.98^{+0.37}_{-0.52}$	2
	24.26	$3.00^{+0.52}_{-0.79}$	1
	24.76	$2.11^{+0.52}_{-0.80}$	1
$2.5 < z \leq 4.5$	25.26	$2.41^{+0.52}_{-0.80}$	2
	26.26	$2.11^{+0.52}_{-0.80}$	1
	26.76	$2.11^{+0.52}_{-0.80}$	1

Note. Numbers in parentheses take into account the effect of the LSS. Errors correspond to 1σ Poisson errors evaluated using the number of sources per bin with redshift determination added in quadrature with the cosmic variance uncertainties. The conversion to units of Mpc^{-3} dex^{-1} used, for example, by Simpson et al. (2012), is done by subtracting $9 - \log(\ln(10))$ from our values.

5.3 RQ AGN

5.3.1 The local LF

The local ($z \lesssim 0.3-0.4$) LF for radio-selected RQ AGN has, so far, never been determined.[5] We present it in Fig. 8. The RQ AGN $z \leq 0.4$ sample (filled squares) includes only six objects and the corresponding LF is therefore quite uncertain. We therefore complement it by deriving the LF for the full sample de-evolved to $z = 0$ (filled circles) using the best-fitting evolutionary parameter from the $\langle V_e/V_a \rangle$ analysis and the local LF derived from the maximum likelihood analysis (double power law, PLE). Given the discussion in Section 4, both these estimates should be reliable. We also plot in Fig. 8 the radio LFs for the 12 μm (open circles) and Center for Astrophysics (CfA; open squares) Seyferts (Rush, Malkan & Edelson 1996) and the Palomar Seyferts (Ulvestad & Ho 2001), that is of the local counterparts of (mostly) RQ AGN. There are a couple of points one needs to consider here. (1) All these LFs are bivariate, that is they were derived by observing in the radio band samples of Seyfert galaxies. Given that the original sample selection was done in the optical, it is almost certain that the samples are not complete in the radio and therefore the LFs are lower limits to the true ones. (2) There is some scatter between the various estimates, although this is usually within the rather large error bars, which are due to the fact that many bins include only 1–2 sources. (3) The high-power ($P \gtrsim 10^{24}$ W Hz^{-1}) tail should not be considered since the 12 μm sample, for example, includes a number of 'classical' RL sources (e.g. 3C 273, 3C 120, OJ 287). Taking all of the above into account, our determination of the local LF for radio-selected RQ AGN is not inconsistent with the Seyfert LFs. We will return to this issue in Section 6.1.2.

[5] In Padovani et al. (2011), we estimated it by de-evolving the full LF to $z = 0$.

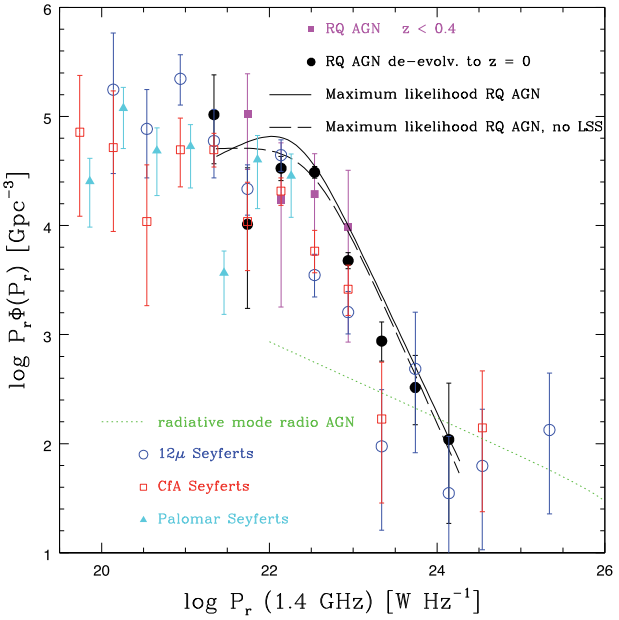

Figure 8. The local differential 1.4 GHz LF for RQ AGN in a $P \times \phi(P)$ form. Filled (magenta) squares indicate the E-CDFS LF at $z \leq 0.4$, while filled (black) circles denote the LF de-evolved to $z = 0$ using the best-fitting evolutionary parameter from the $\langle V_e/V_a \rangle$ analysis. The solid line is the best-fitting double power-law LF from the maximum likelihood method (PLE), while the dashed line is the same LF but taking into account the presence of LSS. The (green) dotted line is the best fit to the local LF of radiative-mode radio AGN (Best et al. 2014). Local bivariate LFs for Seyfert galaxies from three samples are also shown: the 12 μm (open blue circles) and CfA (open red squares) Seyferts (Rush et al. 1996) and the Palomar Seyferts (filled cyan triangles; Ulvestad & Ho 2001). Error bars for the E-CDFS $z \leq 0.4$ sample correspond to 1σ Poisson errors evaluated using the number of sources per bin with redshift determination added in quadrature with the cosmic variance uncertainties.

5.3.2 The LF redshift evolution

The first ever determined evolution of the RQ AGN radio LF is shown in six redshift bins in Fig. 9 (tabulated in Table 6). The

Downloaded from https://academic.oup.com/mnras/article-abstract/452/2/1263/1062981 by guest on 16 April 2020

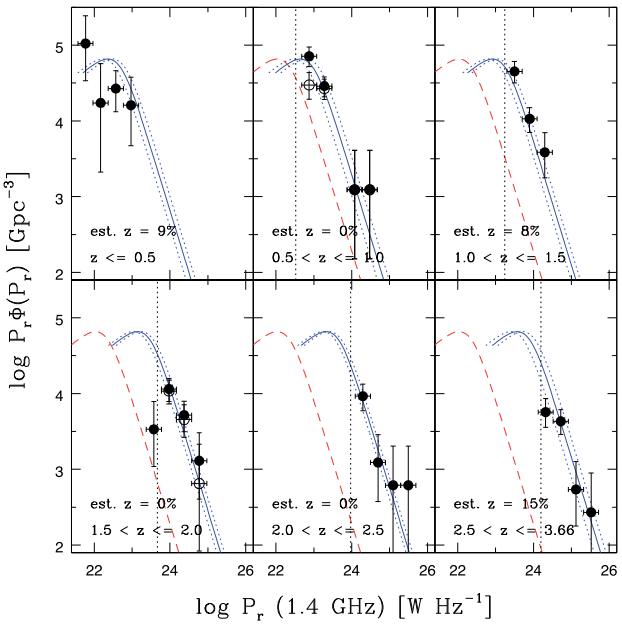

Figure 9. The differential 1.4 GHz LF for RQ AGN in a $P \times \phi(P)$ form in six redshift bins. The (blue) solid lines represent the best-fitting double power-law LF from the maximum likelihood method evolved to the central redshift of the bin using the best fit for PLE $(1+z)^{2.52}$, with dotted lines showing the same LF at the two extreme redshifts defining the bin. The (red) short-dashed line represents the best-fitting LF at $z = 0$. Error bars correspond to 1σ Poisson errors evaluated using the number of sources per bin with redshift determination added in quadrature with the cosmic variance uncertainties. The percentage of redshifts estimated from $f_{3.6\,\mu m}$ is also given for each bin. Open symbols in the $z = 0.5$–1.0 and 1.5–2.0 bins take into account the presence of LSS. The (black) dotted vertical lines denote the completeness limit in power for each redshift range. See the text for details.

increase in power at higher redshifts is clearly visible, as is the fact that the PLE maximum likelihood fit provides a good representation of the LF redshift evolution, which means that the possible slow-down at higher redshifts hinted at in Section 4.2 has to be subtle.

5.4 RL and RQ AGN comparison

Fig. 10 shows the redshift evolution of RL and RQ AGN in various luminosity bins, with the points coming from the $1/V_a$ method and the lines being the best maximum likelihood fits assuming PLE for RQ AGN and PDE for RL AGN, respectively, and a single power law (given the relatively small power range). The figure shows that, while at low powers ($P_{1.4\,GHz} < 10^{23}$ W Hz^{-1}) RQ and RL AGN are equally numerous, the situation changes at $10^{23} < P_{1.4\,GHz} < 10^{25}$ W Hz^{-1}, where RQ AGN overtake RL ones. For example, at $z \sim 2$–3 and $10^{24} < P_{1.4\,GHz} < 10^{25}$ W Hz^{-1}, RQ AGN are more abundant than RL ones by factors of ∼3–10. At even larger powers ($P_{1.4\,GHz} > 10^{25}$ W Hz^{-1}), the number densities of the two classes appear to be similar again but at this point we are running out of RQ AGN.

We stress that the fact that the decline appears to start at larger redshifts for more powerful sources has nothing to do with 'cosmic downsizing' (as instead stated by Simpson et al. 2012) but is simply an effect of our flux density limit. Within a redshift bin, in fact, not all sources in a given radio luminosity bin might be visible by our survey and this leads to a 'loss' of objects. As a result, sources will start to fall below the flux density limit at progressively higher redshifts for larger powers. This explains the sudden stop in the rise of both classes, which in deeper samples is expected to continue (obviously barring an intrinsic redshift cutoff).

Ueda et al. (2014) reach maximum number densities $\sim 3 \times 10^5$ Gpc^{-3} for their X-ray selected (largely RQ) AGN with $10^{42} < L_x < 10^{43}$ erg s^{-1} and $z \sim 0.7$ (see their fig. 12), to be compared with our value of $\sim 7 \times 10^4$ Gpc^{-3} at $z \sim 0.3$ (Fig. 10). This is to be expected as their AGN surface density is ∼3000 versus ∼860 deg^{-2} for our RQ AGN (see Section 6.1.2), which simply means that we have not detected all AGN with $L_x > 10^{42}$ erg s^{-1} (but only those above our radio flux density limit).

Finally, we note that the number densities for 'classical' RL quasars are orders of magnitude smaller than those of our RL AGN ($\lesssim 1$ Gpc^{-3} for $P_{2.7\,GHz} \gtrsim 10^{27}$ W Hz^{-1}: see, e.g., fig. 5 of Wall et al. 2005).

Table 6. LFs of VLA-E-CDFS RQ AGN.

z range	$\log P_{1.4\,GHz}$ (W Hz^{-1})	$\log P\Phi(P)$ (Gpc^{-3})	N
$z \leq 0.5$	21.77	$5.02^{+0.37}_{-0.49}$	2
	22.17	$4.24^{+0.52}_{-0.91}$	1
	22.57	$4.43^{+0.24}_{-0.31}$	5
	22.97	$4.21^{+0.37}_{-0.53}$	3
$0.5 < z \leq 1.0$	22.88	$4.85^{+0.12}_{-0.14}$ ($4.48^{+0.16}_{-0.19}$)	18 (10)
	23.28	$4.46^{+0.12}_{-0.14}$ ($4.43^{+0.12}_{-0.14}$)	20 (19)
	24.08	$3.09^{+0.52}_{-0.91}$	1
	24.48	$3.09^{+0.52}_{-0.91}$	1
$1.0 < z \leq 1.5$	23.50	$4.65^{+0.13}_{-0.15}$	18
	23.90	$4.03^{+0.15}_{-0.18}$	14
	24.30	$3.59^{+0.26}_{-0.33}$	5
$1.5 < z \leq 2.0$	23.57	$3.53^{+0.37}_{-0.49}$	2
	23.97	$4.06^{+0.14}_{-0.16}$ ($4.03^{+0.15}_{-0.17}$)	14 (13)
	24.37	$3.71^{+0.18}_{-0.22}$ ($3.66^{+0.20}_{-0.24}$)	8 (7)
	24.77	$3.11^{+0.37}_{-0.51}$ ($2.81^{+0.52}_{-0.89}$)	2 (1)
$2.0 < z \leq 2.5$	24.29	$3.97^{+0.16}_{-0.19}$	11
	24.69	$3.09^{+0.37}_{-0.52}$	2
	25.09	$2.79^{+0.52}_{-0.91}$	1
	25.49	$2.79^{+0.52}_{-0.91}$	1
$2.5 < z \leq 3.66$	24.32	$3.75^{+0.18}_{-0.20}$	9
	24.72	$3.63^{+0.15}_{-0.17}$	14
	25.12	$2.73^{+0.37}_{-0.48}$	2
	25.52	$2.43^{+0.52}_{-0.83}$	1

Note. Numbers in parentheses take into account the effect of the LSS. Errors correspond to 1σ Poisson errors evaluated using the number of sources per bin with redshift determination added in quadrature with the cosmic variance uncertainties. The conversion to units of Mpc^{-3} dex^{-1} used, for example, by Simpson et al. (2012), is done by subtracting $9 - \log(\ln(10))$ from our values.

6 DISCUSSION

6.1 The evolution of μJy radio sources

We now analyse in more detail the evolution of the two AGN classes and, when applicable, compare it with previous results.

Downloaded from https://academic.oup.com/mnras/article-abstract/452/2/1263/1062981 by guest on 16 April 2020

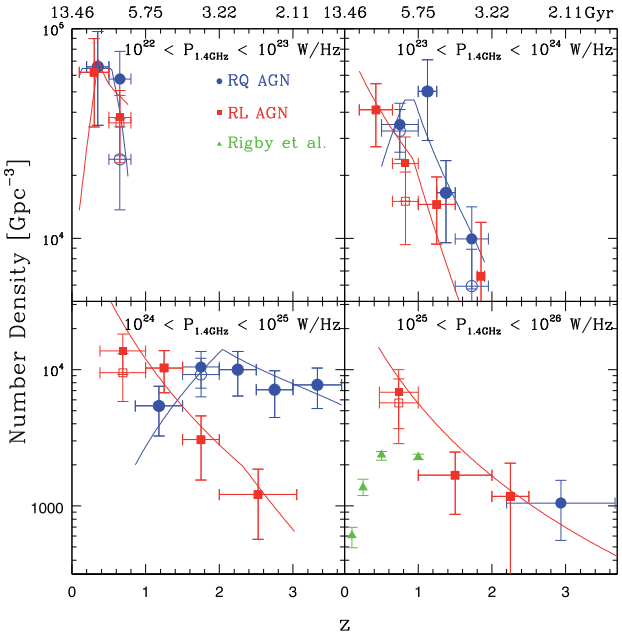

Figure 10. The redshift evolution of RL (red squares) and RQ (blue circles) AGN in various luminosity bins. The top labels refer to cosmic time in Gyr. The points come from the $1/V_a$ method, while the lines are from the best fits assuming a single power law and PLE for RQ AGN and PDE for RL AGN, respectively, taking into account the effect of our flux density limit. Error bars correspond to 1σ Poisson errors added in quadrature with the cosmic variance uncertainties. Open symbols refer to the 'no LSS' samples. Green triangles are from Rigby et al. (2011).

6.1.1 *RL AGN*

The evolution of RL AGN is not described by PLE or a simple PDE. Instead, it can be characterized as a density evolution reaching a peak at $z \sim 0.5$ and then decreasing.

Rigby et al. (2011) studied various samples of *steep-spectrum* ($\alpha_r > 0.5$) AGN selected from a variety of radio surveys with increasingly smaller areas and flux density limits. They found a significant decline in comoving density at $z > 0.7$ for their lower luminosity sources ($10^{25} < P_{1.4\,GHz} < 10^{26}$ W Hz^{-1}). Turnovers were still present at higher powers but moved to larger redshifts, suggesting a luminosity-dependent evolution of the redshift peak, similar to the so-called cosmic downsizing seen, for example, in the X-ray band (Ueda et al. 2014). Fig. 10 (bottom right) shows the relevant points (filled triangles) from fig. 11 of Rigby et al. (2011) in one of the two ranges of luminosities we have in common. Considering that, unlike these authors, we have no cut on α_r and therefore we are bound to have more AGN in our sample, our points agree with theirs within our error bars. The same is true for the 10^{26}–10^{27} W Hz^{-1} range (not shown because there are no RQ AGN at those powers). Fig. 10 shows that at the powers corresponding to the low-luminosity end of the Rigby et al. (2011) sample, we cannot put any constraints on a peak at $z \sim 0.7$, as we are only sensitive to $z \gtrsim 0.5$, but our data are consistent with the trend present in the Rigby et al. (2011) sample. Moreover, we can use fig. 10 of Rigby et al. (2011), which shows a strong correlation between z_{peak} and power. Since our median $P_{1.4\,GHz}$ is $\sim 10^{24}$ W Hz^{-1}, the $z_{peak} \sim 0.5$ we find through the ZDE fit appears to be in agreement with the Rigby et al. (2011) results.

Best et al. (2014) have also studied various samples of (steep-spectrum) radio AGN selected from a variety of surveys with increasingly smaller areas and flux density limits. They classify their sources into radiative-mode and jet-mode AGN using emission line diagnostics. Based on Fig. 6, Bonzini et al. (2013), and Section 6.2 (see also fig. 1 of Best et al. 2014), the large majority of our RL AGN have to be of the latter type, so we compare our findings to their results on the jet-mode population. For $P_{1.4\,GHz} \lesssim 10^{24}$ W Hz^{-1}, Best et al. (2014, see their fig. 5) find that its space density stays constant up to $z \approx 0.5$ and then decreases to $z = 1$. At moderate powers, $10^{24} \lesssim P_{1.4\,GHz} \lesssim 10^{26}$ W Hz^{-1}, the space density increases to $z \sim 0.5$ before falling. At the highest powers, the space density appears to increase up to $z \sim 1$ but the statistics is somewhat limited.

Our results are similar to those of Best et al. (2014), taking into account our somewhat more limited coverage of the luminosity–redshift plane. Fig. 10 shows that for $P_{1.4\,GHz} \lesssim 10^{23}$ W Hz^{-1}, the space density of RL AGN increases up to $z \approx 0.5$, while for $10^{24} \lesssim P_{1.4\,GHz} \lesssim 10^{26}$ W Hz^{-1}, and taking into account the effect of the LSS, it increases to $z \approx 1.0$ before falling. We cannot say anything about larger powers.

It is important to stress the difference between a 'purely flux density-limited' sample, like ours, and many others published in the literature, which are very often put together by cross-correlating very large surveys. For example, the Best et al. (2014) LF, as discussed in Heckman & Best (2014), is built by combining four different radio LFs based on four spectroscopic samples: Las Campanas (Machalski & Godlowski 2000), 2dFGRS (Sadler et al. 2002), SDSS/NVSS/FIRST (Best & Heckman 2012), and 6dFGS (Mauch & Sadler 2007). Although these samples are large (including, e.g., more than 2500 and 7000 sources for the 6dFGS and SDSS/NVSS/FIRST samples), one needs to consider that, by construction, they do not sample the full RL AGN population. All of them, in fact, are limited to galaxies (and therefore do not include non-stellar and broad-line sources) and to steep-spectrum ($\alpha_r > 0.5$) radio sources. Gendre et al. (2010, 2013), who derived the LF for FR I/II radio galaxies, also included only galaxies, excluding any compact or quasar-dominated source. Our LF, being simply radio flux density limited, has no such biases and therefore is bound to find number densities larger than these determinations; this is true also for Mao et al. (2012) and Simpson et al. (2012) (pending their different definition of RL AGN).

Padovani et al. (2011) made a connection between the negative evolution of RL AGN and that of elliptical galaxies. For example, Taylor et al. (2009) have found that the number density of massive ($M_\star > 10^{11}\,M_\odot$) red galaxies declines with redshift as $\Phi(z) \propto (1+z)^{-1.60 \pm 0.14(\pm 0.21)}$ for $z \leq 1.8$.[6] If we restrict our sample to $z \leq 1.8$, we get $\Phi(z) \propto (1+z)^{-1.3 \pm 0.5}$, which is very similar.

Fig. 11 compares the LF of our RL AGN in the redshift range 1.3–1.7 with two different models at $z = 1.5$ from Best et al. (2014). These models, starting from the assumption that jet-mode RL AGN are hosted in quiescent galaxies, combine the known stellar mass function of the host galaxies with the stellar mass dependence of the presence of a RL AGN to make predictions on the evolution of the RL AGN LF. Model 2b is a luminosity–density evolution model, in which the luminosity of the RL AGN increases with increasing redshift and there is a delay of ~2 Gyr between the formation of the host galaxy and the presence of a radio jet. Model 3a is a PDE model in which a subset of the sources classified as jet mode are in reality

[6] Best et al. (2014) have compiled some more recent results, which paint a somewhat more complex evolution.

Downloaded from https://academic.oup.com/mnras/article-abstract/452/2/1263/1062981 by guest on 16 April 2020

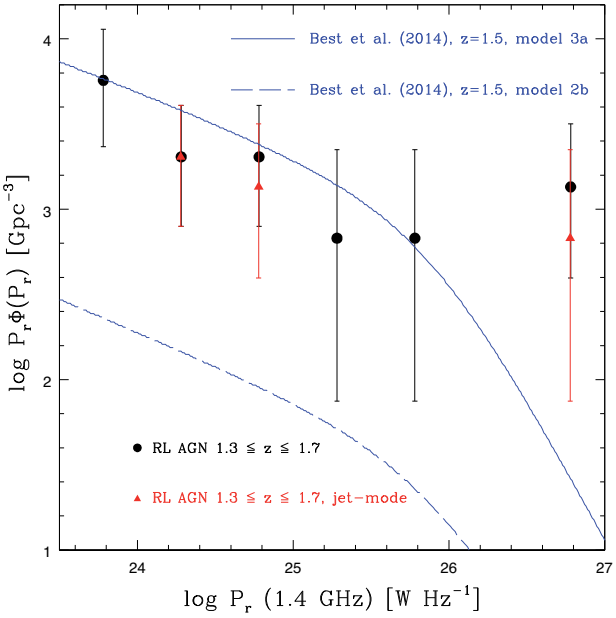

Figure 11. The RL AGN LF at $1.3 \leq z \leq 1.7$ compared with two different models from Best et al. (2014) at $z = 1.5$. Filled (black) circles include all sources, while (red) triangles represent our best estimate of the jet-mode LF. See the text for details.

related to the radiative-mode RL AGN population. This could be due to a misclassification of some objects or to a change in physical properties with redshift. As shown in fig. 7 of Best et al. (2014), the LFs predicted by these models are clearly distinguishable only at $z > 1$, i.e. beyond their maximum redshift. Our sample covers a wide radio power range also at $z \sim 1.5$, and therefore we have the opportunity to test these different models. As shown in Fig. 11, model 3a is consistent with our LF, while model 2b is clearly not. Since the predictions were based on jet-mode-only RL AGN, we also restricted our sample only to these type of sources by following Bonzini et al. (2013) and using the 22 μm power criterion proposed by Gürkan et al. (2014).[7] Only one of our jet-mode RL AGN turned out to have an Eddington ratio inconsistent with this classification (>0.1; see Section 6.2) and was therefore re-classified. The jet-mode LF is shown in Fig. 11 (filled red triangles) and is basically the same as the overall LF.

6.1.2 *RQ AGN*

We have provided a more robust estimate of the evolution of RQ AGN in the radio band, following upon the first one derived in Padovani et al. (2011). We have modelled it as a PLE $P(z) \propto (1+z)^{k_L}$, obtaining $k_L = 3.0 \pm 0.2$ from the V_e/V_a analysis and $k_L = 2.5 \pm 0.2$ from the maximum likelihood one, in both cases over the 0.2–3.66 redshift range.

The redshift evolution of X-ray selected (largely RQ) AGN is best described by a more complex evolutionary model, the so-called luminosity-dependent density evolution, which takes into account the observed steepening with redshift in the faint-end slope of the LF and the fact that luminosity evolution appears to stop at $z \approx 2.5$, as shown, for example, in fig. 11 of Ueda et al. (2014). It is important to note that the latter LF, and all those studied in the X-ray band, refers only to Compton-thin AGN, characterized by an absorbing column density $N_H < 1.5 \times 10^{24}$ cm^{-2}, while in principle we have no such limitation (although our cut in X-ray power might also exclude Compton-thick sources). Keeping that in mind, Fig. 9 shows that the LF faint-end slope is constrained only at $z < 0.5$; moreover, most (∼74 per cent) of our RQ AGN have $z < 2$. The two effects combined make any deviation from PLE of the type seen in the X-ray band hard to detect.

We nevertheless split the RQ AGN sample into two sub-samples of the same size with redshift, respectively, smaller and larger than 1.3, fitting PLE evolution to both. Evolution slows down at higher redshifts, with $k = 4.0 \pm 0.6$ and 2.0 ± 0.5, respectively, below and above $z = 1.3$. However, the errors on the evolutionary parameters overlap at the $\sim 2\sigma$ level, making this difference not statistically significant. In other words, a high-redshift slowing down of the evolution is consistent with, but not required by, our data.

We note that the surface density of our RQ AGN, ∼860 deg^{-2}, is already larger than that reached by the deepest optical surveys, that is ∼670 deg^{-2} for type I and II combined. This number is the sum of ∼200 deg^{-2}, from a type II AGN sample based on the zCOSMOS survey and selected on the basis of the optical emission line ratios (Bongiorno et al. 2010), and ∼470 deg^{-2}, from a type I AGN sample extracted from the VIMOS VLT Deep Survey (Gavignaud et al. 2006). We note that the overall (RQ plus RL) AGN surface density is ∼1500 deg^{-2}.

As regards the X-ray band, our RQ AGN surface density is ∼20 times smaller than that of Lehmer et al. (2012), which is simply due to the fact that our radio flux density limit is still not as deep as the equivalent one in the X-rays (see also fig. 10 in Vattakunnel et al. 2012, for a comparison of the star formation rates reachable in the two bands).

To allow for a fairer comparison[8] between our sample and the X-ray samples, we have fitted a double power-law LF to all points in Fig. 8, obtaining $N_T \sim 2.7 \times 10^5$ Gpc^{-3}, a value, which is basically the same as the maximum number density of Ueda et al. (2014). This implies a surface density ∼15 400 deg^{-2} (using equation 2 of Padovani 2011), to be compared with ∼15 000 deg^{-2} in the 4 Ms survey of Lehmer et al. (2012). In other words, once one takes into account the fact that our radio flux density limit is still not as deep as the equivalent one in the X-ray band by including the radio LF of Seyfert galaxies, the number and surface densities one obtains are the same, which shows that we are simply looking at the same population from two different bands and the sources we are selecting in the radio band are the same as the X-ray emitting AGN.

6.2 Astrophysics of μJy sources

To analyse in more depth the astrophysical nature of our AGN, we study the ratio of X-ray power to stellar mass, $L_x/M_\star$, a proxy for the Eddington ratio L/L_{Edd} (see, e.g., Bongiorno et al. 2012). This can in fact be written as

$$\frac{L}{L_{Edd}} = \frac{k_{bol}}{1.26 \times 10^{38} \Upsilon} \times \frac{L_x}{M_\star}, \quad (2)$$

where k_{bol} is the 2–10 keV bolometric correction and $\Upsilon = M_{BH}/M_\star$ is the ratio between black hole and stellar mass.

[7] As discussed in Bonzini et al. (2013), this method has not been tested on as faint a sample as ours and therefore we regard this as only a rough classification.

[8] Some of the topics discussed here and in Section 6.3 were originally presented in Padovani (2011). We give here updated numbers.

Downloaded from https://academic.oup.com/mnras/article-abstract/452/2/1263/1062981 by guest on 16 April 2020

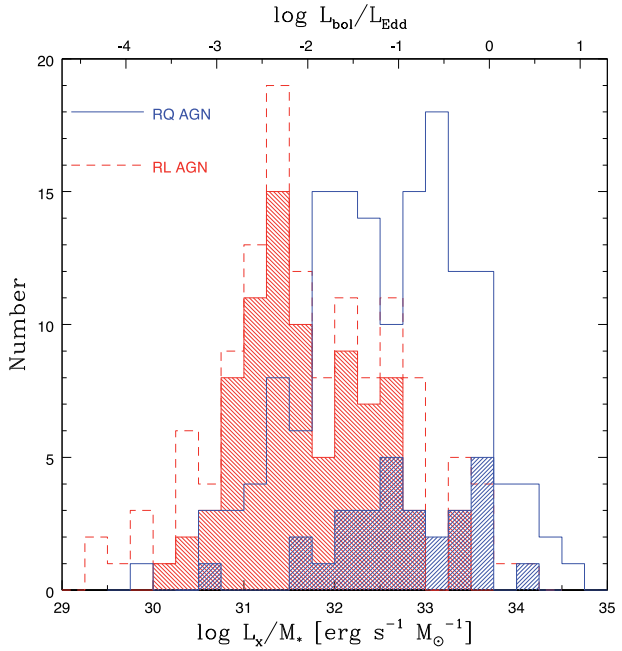

Figure 12. The distribution of the ratio of X-ray power to stellar mass, $L_{\rm x}/M_\star$ for RQ (blue solid histogram) and RL (red dashed histogram) AGN. The top labels give the approximate values of the Eddington ratio. Shaded areas are upper limits.

Stellar masses were estimated by Bonzini et al. (2013), using the method of Bongiorno et al. (2012). Fig. 12 displays the distribution of $L_{\rm x}/M_\star$ for RQ (blue solid histogram) and RL (red dashed histogram) AGN, with shaded areas denoting upper limits. We assume $k_{\rm bol} = 25$ (Bongiorno et al. 2012) and $\Upsilon = 0.001$ (Trump et al. 2015, and references therein), noting that, given the observational scatter and a possible dependence of $k_{\rm bol}$ on $L/L_{\rm Edd}$, the resulting $L/L_{\rm Edd}$ values are only approximate. These are given by the top labels in Fig. 12. For our choice of parameters, $L_{\rm x}/M_\star = 5 \times 10^{33}$ erg s^{-1} M$_\odot^{-1}$ corresponds to the Eddington limit.

Fig. 12 shows that the two $L_{\rm x}/M_\star$ distributions appear very different, with RQ AGN having much larger values. Given the substantial fraction of upper limits (all on $L_{\rm x}$), we used ASURV (Lavalley, Isobe & Feigelson 1992), the survival analysis package which employs the routines described in Feigelson & Nelson (1985) and Isobe, Feigelson & Nelson (1986), which evaluate mean values by dealing properly with non-detections and also compute the probability that two samples are drawn from the same parent population. RQ and RL AGN have totally different (p-values < 0.001) distributions, according to all two-sample tests in ASURV. The means are also very different, being $L_{\rm x}/M_\star \sim 2.4 \times 10^{32}$ and $\sim 5.5 \times 10^{30}$ erg s^{-1} M$_\odot^{-1}$ for RQ and RL AGN, respectively, a factor of $\sim$40 difference. The corresponding (approximate) Eddington ratios are $\approx$0.05 and $\approx$0.001. Given that the dividing line between radiative- and jet-mode sources is thought to be $L/L_{\rm Edd} \approx 0.01$ (e.g. Heckman & Best 2014), our results are consistent with our RQ and RL AGN being mostly of the former and latter type, respectively.

6.3 The intrinsic fraction of radiative-mode RL AGN

The RL AGN fraction, $f_{\rm RLAGN}$, has been derived in the past from bright, optically selected samples which contain RL sources very different from most of the sources studied here. Namely, they are RL quasars and therefore belong with the radiative-mode AGN, while we have mostly jet-mode objects (Section 6.2). Indeed, the RL AGN in the 'classic' Palomar Green sample studied by Kellermann et al. (1989), from which the 'standard' value $f_{\rm RLAGN} \sim 10$ per cent comes,[9] have $P_{\rm 5\,GHz} \gtrsim 10^{25}$ W Hz^{-1} and maximum number densities $P\Phi(P) \sim 11$ Gpc^{-3} (Padovani 1993), that is they are below the plotting area in Figs 5 and 6 and barely inside in Fig. 8.

The way this fraction was derived was by looking for a bimodality in the radio-to-optical flux density ratio, R, classifying as RL the sources with R larger than the value corresponding to the minimum in the distribution ($0.1 < R < 100$ in Kellermann et al. 1989).[10] Padovani (2011) has pointed out that: (a) bright, optically selected samples might include RL quasars with their optical flux boosted by relativistic beaming (e.g. Goldschmidt et al. 1999), which artificially increases their fraction; (b) RL AGN are on average more powerful than RQ ones in the optical band (e.g. Zamfir, Sulentic & Marziani 2008). When one reaches the very faint end of the optical LF, only RQ AGN will be present and therefore the integrated, intrinsic RL fraction will be quite small. Both of these effects lead to an overestimate of the RL AGN fraction when using the 'standard' method. Indeed, it has been known for some time that the RL fraction drops with decreasing optical luminosity (Padovani 1993). Jiang et al. (2007) have also shown that the fraction of RL quasars at $z = 0.5$ declines from 24 to 6 per cent as luminosity decreases from $M_{2500} = -26$ to -22. In other words, the usually quoted value refers to the bright part of the LF and, when integrated over the full range of powers, the resulting $f_{\rm RLAGN}$ is much smaller.

The best way to approach the question of the *intrinsic* value of $f_{\rm RLAGN}$ is to look at the band under discussion, namely the radio one. We plot in Fig. 8 our best estimate(s) of the local LF for RQ (radiative-mode) AGN, together with the $z < 0.3$ LF of radiative-mode RL AGN from Best et al. (2014, dotted line). One can see that the fraction of radiative-mode RL AGN is a strong function of radio power, as the shape of the two LFs is very different. In particular, for $P_{\rm 1.4\,GHz} \gtrsim 10^{24}$ W Hz^{-1}, radiative-mode RL AGN dominate and $f_{\rm RLAGN} \gtrsim 0.5$, while for $P_{\rm 1.4\,GHz} \geq 10^{22}$ W Hz^{-1}, which is the limiting value for radiative-mode RL AGN, $f_{\rm RLAGN} \sim 0.04$ (where we have used the double power-law fit derived in the previous subsection). To derive the overall intrinsic value, one would need to integrate down to lower values but we do not yet have a handle on the low-end of the radiative-mode RL AGN LF.

Our RQ AGN include absorbed (type II) and unabsorbed (type I) sources, while the LF of radiative-mode RL AGN from Best et al. (2014) is limited to radio galaxies and steep-spectrum radio sources (Section 6.1.1). However, as radio quasars are relativistically beamed, they tend to be much more luminous and less numerous than radio galaxies and therefore we believe that down to $P_{\rm 1.4\,GHz} \sim 10^{22}$ W Hz^{-1} their exclusion makes very little difference.

We note that if one takes as dividing line between RQ and radiative-mode RL AGN the power at which the two LFs cross, one gets $P_{\rm 1.4\,GHz} \approx 10^{24}$ W Hz^{-1} at $z \sim 0$, i.e. the same dividing value between the two classes that has been suggested in the past (see section 2 of Padovani 1993). Given the strong redshift

[9] Although in that paper the quoted value is 15–20 per cent.

[10] We obviously cannot study the R distribution to look for a possible bimodality as our RL AGN are mostly jet-mode sources while our RQ AGN are mostly radiative-mode sources (see Section 6.2). Furthermore, as discussed by Padovani et al. (2009) and Padovani (2011), R is useful for quasar samples, where it is related to the jet/disc ratio, but loses its meaning for radio galaxies.

Downloaded from https://academic.oup.com/mnras/article-abstract/452/2/1263/1062981 by guest on 16 April 2020

evolution of both LFs, one can predict that this power is redshift dependent and will get larger at higher redshifts, as indeed appears to be the case (Padovani 1993). Future radio studies of deeper/wider samples, which will include RL AGN of the jet-mode and radiative-mode type, should be able to study the RL fraction dependence on redshift by deriving the evolving LFs for both classes.

7 SUMMARY AND CONCLUSIONS

We have used a deep, complete radio sample of 680 objects down to a 1.4 GHz flux density of 32.5 μJy selected in the E-CDFS area to derive the number counts of the various sub-mJy classes and to study in detail the evolution and LFs of radio-faint AGN up to $z \sim 4$. Our main results can be summarized as follows.

(i) What we consider to be the best determination of the source population of the sub-mJy radio sky shows that SFGs and AGN make up a roughly equal part of the sub-mJy sky down to 32.5 μJy, with the former becoming the dominant population only below ∼0.1 mJy. RQ AGN are confirmed to be an important class of sub-mJy sources, accounting for ∼25 per cent of the sample and ∼60 per cent of all AGN, and outnumbering RL AGN at $\lesssim$0.1 mJy (Section 3).

(ii) The AGN that make up the faint radio sky consist of two totally distinct populations: RQ AGN, mostly of the radiative-mode type, and RL AGN, largely of the jet-mode kind, characterized by very different evolutions, LFs, and Eddington ratios (Sections 5 and 6).

(iii) RQ AGN evolve in radio power as $\propto (1+z)^{2.5}$, similarly to SFGs, up to $z \sim 4$ but with a hint of a slowing down above $z \sim 1.3$. Their LF is steep ($\Phi(P) \propto P^{-2.5}$ for $P \gtrsim 2 \times 10^{22}$ W Hz^{-1}) and their $L/L_{\rm Edd}$ is typically $\gtrsim$0.01 (Table 3 and Sections 6.1.2 and 6.2).

(iv) RL AGN evolve in number $\propto (1+z)^2$ but only up to $z \sim 0.5$, beyond which their number density declines steeply $\propto (1+z)^{-4}$. Their LF is flat ($\Phi(P) \propto P^{-1.4}$) and their $L/L_{\rm Edd}$ is typically $\lesssim$0.01 (Table 4 and Sections 6.1.1 and 6.2).

(v) The first determination of the local radio LF of RQ AGN appears to be consistent with that of Seyferts. Putting the two together, one derives a number density of RQ AGN equivalent to that of X-ray selected AGN, which shows that we are looking at the same population from two different bands (Sections 5.3.1 and 6.1.2).

(vi) We have approached the question of the *intrinsic* value of the fraction of radiative-mode RL sources, $f_{\rm RLAGN}$, within the AGN population by using, for the first time, the radio band (while all previous attempts were normally done in the optical band). By combining the local radio LF of Seyferts and our RQ AGN with a previously published estimate of the LF of radiative-mode RL AGN, we find that for $P_{1.4\,\rm GHz} \gtrsim 10^{24}$ W Hz^{-1} RL AGN dominate and $f_{\rm RLAGN} \gtrsim 0.5$, while down to $P_{1.4\,\rm GHz} \sim 10^{22}$ W Hz^{-1} $f_{\rm RLAGN} \sim 4$ per cent (Section 6.3).

(vii) The surface density of radio-selected, RQ AGN, ∼860 deg^{-2}, is already larger than that reached by the deepest optical surveys. This means that sub-mJy radio surveys, given the appropriate ancillary multiwavelength data, have already the potential of detecting large numbers of RQ AGN bypassing the problems of obscuration, which plague the optical and soft X-ray bands (Section 6.1.2).

In an upcoming paper (Padovani et al., in preparation), we will discuss in detail the evolution and LF of the SFG in our sample and how they compare to those of RQ AGN, which is very relevant for the issue of the mechanism behind radio emission in RQ AGN (see also Padovani et al. 2011 and Bonzini et al. 2015, submitted).

ACKNOWLEDGEMENTS

We thank Philip Best, Ed Fomalont, Rachel Somerville, Jasper Wall, and an anonymous referee for helpful comments and discussions and Piero Rosati and Shaji Vattakunnel for their work on the E-CDFS survey. We acknowledge the ESO/GOODS project for the ISAAC and FORS2 data obtained using the Very Large Telescope at the ESO Paranal Observatory under programme ID(s): LP168.A-0485, 170.A-0788, 074.A-0709, 275.A-5060, and 081.A-0525. We made use of the TOPCAT software package (Taylor 2005). The VLA is a facility of the National Radio Astronomy Observatory which is operated by Associated Universities, Inc., under a cooperative agreement with the National Science Foundation. This research has made use of NASA's Astrophysics Data System (ADS) Bibliographic Services.

REFERENCES

Avni Y., Bahcall J. N., 1980, ApJ, 235, 694
Best P. N., Heckman T. M., 2012, MNRAS, 421, 1569
Best P. N., Ker L. M., Simpson C., Rigby E. E., Sabater J., 2014, MNRAS, 445, 955
Bongiorno A. et al., 2010, A&A, 510, A56
Bongiorno A. et al., 2012, MNRAS, 427, 3103
Bonzini M. et al., 2012, ApJS, 203, 15
Bonzini M., Padovani P., Mainieri V., Kellermann K. I., Miller N., Rosati P., Tozzi P., Vattakunnel S., 2013, MNRAS, 436, 3759
Condon J. J., 1984, ApJ, 287, 461
Condon J. J., 1997, PASP, 109, 166
Condon J. J. et al., 2012, ApJ, 758, 23
Del Moro A. et al., 2013, A&A, 549, A59
Donley J. L. et al., 2012, ApJ, 748, 142
Dunlop J. S., Peacock J. A., 1990, MNRAS, 247, 19
Dunlop J. S., McLure R. J., Kukula M. J., Baum S. A., O'Dea C. P., Hughes D. H., 2003, MNRAS, 340, 1095
Fanaroff B. L., Riley J. M., 1974, MNRAS, 167, 31P
Feigelson E. D., Nelson P. I., 1985, ApJ, 293, 192
Gavignaud I. et al., 2006, A&A, 457, 79
Gehrels N., 1986, ApJ, 303, 336
Gendre M. A., Best P. N., Wall J. V., 2010, MNRAS, 450, 1719
Gendre M. A., Best P. N., Wall J. V., Ker L. M., 2013, MNRAS, 430, 3086
Gilli R. et al., 2003, ApJ, 592, 721
Goldschmidt P., Kukula M. J., Miller L., Dunlop J. S., 1999, ApJ, 511, 612
Gürkan G., Hardcastle M. J., Jarvis M. J., 2014, MNRAS, 438, 1149
Heckman T. M., Best P. N., 2014, ARA&A, 52, 589
Huynh M. T., Hopkins A. M., Lenc E., Mao M. Y., Middelberg E., Norris R. P., Randall K. E., 2012, MNRAS, 426, 2342
Isobe T., Feigelson E. D., Nelson P. I., 1986, ApJ, 306, 490
Isobe T., Feigelson E. D., Akritas M. G., Babu G. J., 1990, ApJ, 364, 104
Jiang L., Fan X., Ivezić Ž., Richards G. T., Schneider D. P., Strauss M. A., Kelly B. C., 2007, ApJ, 656, 680
Kellermann K. I., Sramek R., Schmidt M., Shaffer D. B., Green R., 1989, AJ, 98, 1195
Kellermann K. I., Fomalont E. B., Mainieri V., Padovani P., Rosati P., Shaver P., Tozzi P., Miller N., 2008, ApJS, 179, 71
Lavalley M., Isobe T., Feigelson E., 1992, in Worrall D. M., Biemesderfer C., Barnes J., eds, ASP Conf. Ser. Vol. 25, Astronomical Data Analysis Software and Systems I. Astron. Soc. Pac., San Francisco, p. 245
Lehmer B. D. et al., 2012, ApJ, 752, 46
McAlpine K., Jarvis M. J., Bonfield D. G., 2013, MNRAS, 436, 1084
Machalski J., Godlowski W., 2000, A&A, 360, 463
Mainieri V. et al., 2008, ApJS, 179, 95
Mao M. Y. et al., 2012, MNRAS, 426, 3334
Mauch T., Sadler E. M., 2007, MNRAS, 375, 931

Downloaded from https://academic.oup.com/mnras/article-abstract/452/2/1263/1062981 by guest on 16 April 2020

Miller N. A., Fomalont E. B., Kellermann K. I., Mainieri V., Norman C., Padovani P., Rosati P., Tozzi P., 2008, ApJS, 179, 114
Miller N. A. et al., 2013, ApJS, 205, 13
Morris S. L., Stocke J. T., Gioia I. M., Schild R. E., Wolter A., Maccacaro T., Della Ceca R., 1991, ApJ, 380, 49
Moster B. P., Somerville R. S., Newman J. A., Rix H.-W., 2011, ApJ, 731, 113
Muxlow T. W. B. et al., 2005, MNRAS, 358, 1159
Padovani P., 1993, MNRAS, 263, 461
Padovani P., 2011, MNRAS, 411, 1547
Padovani P., Giommi P., Landt H., Perlman E. S., 2007, ApJ, 662, 182
Padovani P., Mainieri V., Tozzi P., Kellermann K. I., Fomalont E. B., Miller N., Rosati P., Shaver P., 2009, ApJ, 694, 235
Padovani P., Miller N., Kellermann K. I., Mainieri V., Rosati P., Tozzi P., 2011, ApJ, 740, 20
Padovani P., Bonzini M., Miller N., Kellermann K. I., Mainieri V., Rosati P., Tozzi P., Vattakunnel S., 2014, in Mickaelian A., Aharonian F., Sanders D., eds, Proc. IAU Symp. 304, Multiwavelength AGN Surveys and Studies. Cambridge Univ. Press, Cambridge, p. 79
Rigby E. E., Best P. N., Brookes M. H., Peacock J. A., Dunlop J. S., Röttgering H. J. A., Wall J. V., Ker L., 2011, MNRAS, 416, 1900
Rush B., Malkan M. A., Edelson R. A., 1996, ApJ, 473, 130
Ryle M., Scheuer P. A. G., 1955, Proc. R. Soc. A, 230, 448
Sadler E. M. et al., 2002, MNRAS, 329, 227
Sandage A., 1965, ApJ, 141, 1560
Schmidt M., 1963, Nature, 197, 1040
Schmidt M., 1968, ApJ, 151, 393
Simpson C. et al., 2012, MNRAS, 421, 3060
Smolčić V. et al., 2009, ApJ, 696, 24
Somerville R. S., Lee K., Ferguson H. C., Gardner J. P., Moustakas L. A., Giavalisco M., 2004, ApJ, 600, L171
Taylor M. B., 2005, in Shopbell P., Britton M., Ebert R., eds, ASP Conf. Ser. Vol. 347, Astronomical Data Analysis Software and Systems XIV. Astron. Soc. Pac., San Francisco, p. 29
Taylor E. N. et al., 2009, ApJ, 694, 1171
Tozzi P. et al., 2009, ApJ, 698, 740
Trump J. R. et al., 2015, ApJ, preprint (arXiv:1501.02801)
Ueda Y., Akiyama M., Hasinger G., Miyaji T., Watson M. G., 2014, ApJ, 786, 104
Ulvestad J. S., Ho L. C., 2001, ApJ, 558, 561
Vattakunnel S. et al., 2012, MNRAS, 420, 2190
Vernstrom T., Norris R. P., Scott D., Wall J. V., 2015, MNRAS, 447, 2243
Wall J. V., Jenkins C. R. 2012, Practical Statistics for Astronomers. Cambridge Univ. Press, Cambridge, UK, p. 194
Wall J. V., Jackson C. A., Shaver P. A., Hook I. M., Kellermann K. I., 2005, A&A, 434, 133
White S. V., Jarvis M. J., Häußler B., Maddox N., 2015, MNRAS, 448, 2665
Zamfir S., Sulentic J. W., Marziani P., 2008, MNRAS, 387, 856

APPENDIX A: REDSHIFT ESTIMATES

As shown in Fig. A1, reasonable and secure redshifts (i.e. spectroscopic with quality flag $\geq$2, as defined in Bonzini et al. 2012) are strongly correlated with $f_{3.6\,\mu m}$, albeit with some scatter in particular at low redshift. The best and simplest approach to estimate the redshift for the $\sim$8 per cent of the objects in the sample without observed redshift is then to derive it from their $f_{3.6\,\mu m}$ by using the relationship shown in the figure (solid line), that is $\log z = -0.677 \log f_{3.6\,\mu m} + 1.185$. This was derived applying the ordinary least-squares bisector method (Isobe et al. 1990), which treats the variables symmetrically, to the $z \geq 0.3$ sample. The low-redshift cut was applied for three reasons: (1) in order to reduce the scatter in the input data; (2) because the maximum $f_{3.6\,\mu m}$ of the sources without redshift is $\sim$200 μJy, which corresponds to

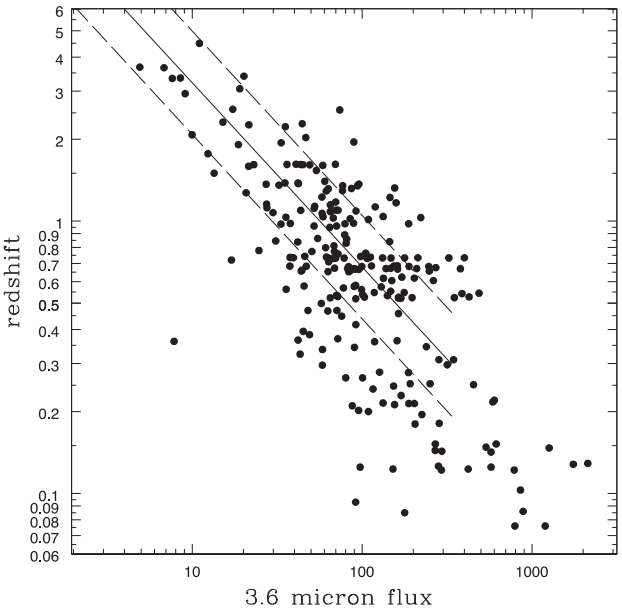

Figure A1. Redshift versus 3.6 μm flux density (in μJy) for our sources with reasonable and secure redshift information (quality flag $\geq$2 as defined in Bonzini et al. 2012). The solid line is the best fit for $z \geq 0.3$, while the dashed lines represent the rms error. See the text for details.

$z \sim 0.3$ deriving the best fit for the whole sample; (3) because the median $f_{3.6\,\mu m}$ for sources without redshift is $\sim$10 μJy and therefore they should typically be at large ($z > 1$) redshift; inclusion of the low-redshift sources in the sample might therefore bias our estimates. We note that the best fits for the different sub-classes give redshift values, which differ only by $\sim$0.4 for sources having $f_{3.6\,\mu m} \sim 10$ μJy (the median for sources without redshift). Note also that for $f_{3.6\,\mu m} = 1$ μJy, the minimum value for the sample, $z \sim 15.3$, which is on the high side. We therefore set the maximum redshift equal to the maximum observed values (spectroscopic or photometric) for the three sub-classes, namely $z \sim 4.7$, 7.0, and 4.5 for SFGs, RQ, and RL AGN, respectively.

APPENDIX B: THE LSS OF THE E-CDFS

Gilli et al. (2003) have studied the LSS in the CDFS in the X-ray band, finding two main, narrow ($\Delta z \lesssim 0.02$) structures at $z = 0.67$ and 0.73 and other spikes at 1.04, 1.62, and 2.57. Indeed, the redshift distributions shown in Fig. 2 peak in the 0.5–0.75 bin for all classes. Given the small area of our survey one could worry that such redshift spikes might influence some of our results. We then studied the LSS of the E-CDFS by looking for narrow ($\Delta z \sim 0.01$–0.03) structures and smoothing the observed spectroscopic redshift distribution in large ($\Delta z \sim 0.1$–0.3) bins to estimate the background distribution. Redshift peaks were defined as spikes being $>2\sigma$ higher than the background for Poissonian errors. Applying this procedure to the whole sample we recovered the main structures of Gilli et al. (2003), namely those at $z \sim 0.67$, 0.73, and 1.62. We also find a structure at $z = 0.52$, present in the near-IR band data of Gilli et al. (2003), and a new one at $z \sim 0.12$. Studying the LSS for the various sub-classes, however, showed that not all redshift peaks are present for all classes. We then studied the LSS individually finding the following significant peaks: (1) SFGs: 0.122–0.126 and 0.729–0.736; AGN: 0.521–0.537, 0.661–0.686, 0.720–0.738,

Downloaded from https://academic.oup.com/mnras/article-abstract/452/2/1263/1062981 by guest on 16 April 2020

and 1.603–1.619; RQ AGN: 0.521–0.529, 0.652–0.671, and 1.591–1.619; RL AGN: 0.675–0.686 and 0.731–0.734. We then created 'no LSS' sub-samples by removing the sources in the bins listed above in excess of the background distribution. The selection of the sources to be kept, which typically included ∼20 per cent of those in the bin, was done by picking the object(s) with radio flux densities closest to the median value of the bin.

This paper has been typeset from a TEX/LATEX file prepared by the author.

Downloaded from https://academic.oup.com/mnras/article-abstract/452/2/1263/1062981 by guest on 16 April 2020